A Herschel/HIFI study of Water in Two Intermediate-Mass Star Forming Regions: Vela IRS 17 and Vela IRS 19

by

Samuel Tisi

A thesis
presented to the University of Waterloo
in fulfilment of the
thesis requirement for the degree of
Master of Science
in
Physics

Waterloo, Ontario, Canada, 2013

I hereby declare that I am the sole author of this thesis. This is a true copy of the thesis, including any required final revisions, as accepted by my examiners.

I understand that my thesis may be made electronically available to the public.

Abstract

While the single core accretion model for low mass star formation is well developed, it cannot simply be extended into the high mass star formation regime where clustered star formation dominates. The study of intermediate-mass star formation should provide us with insights into how the process of star formation changes for high mass stars. In this thesis observations of H_2O line emission from two intermediate-mass candidate Young Stellar Objects (YSOs) made using the HIFI instrument aboard the Herschel Space Observatory are presented. Modelling of molecular line emission using the radiative transfer code RATRAN is used to put constraints on kinematics and the abundance of water throughout the region by modelling the observed water lines after decomposing them into separate Gaussian components. The medium component of the 752 GHz line from Vela IRS 17 was modelled by using a turbulent velocity of 1.7 km s $^{-1}$ and an outer abundance of 6×10^{-8}. The narrow component of the 752 GHz line from Vela IRS 19 could be modelled using a turbulent velocity of 0.6 km s $^{-1}$ and an outer abundance of 6×10^{-8}, while the medium component required an outer abundance of 4×10^{-7} with a turbulent velocity of 2.5 km s^{-1}. The constraints on water abundance in these star-forming regions are to be used along with studies of water in low and high mass star-forming regions in the effort to improve our understanding of star formation across the entire stellar mass spectrum.

Acknowledgements

I would like to give my deepest thanks to Dr. Michel Fich for the opportunity to work with him on this research. I would like to extend my most sincere gratitude to both him and Dr. Carolyn M^{c}Coey for their guidance and support throughout my work.

Dedication

It has been said that humanity is a piece of the Universe experiencing itself subjectively. As science is one approach to developing and expanding humanity's understanding of the Universe, I dedicate this work to the Universe's continued exploration into itself, as well as to my mother, Jaye Dee Cawood.

Contents

List of Figures

List of Tables

Chapter 1

Introduction

Stars are large, luminous, gravitationally bound spheres of hot gas. Their luminosity lights up the galaxy, providing much of the energy that illuminates the less luminous features such as large molecular clouds of gas. Studying other galaxies in the universe is also possible because of stars. Galaxies don't always exhibit spiral arms or even a strictly planar geometry; stars highlight a galaxy's structure, making it possible to develop a more complete picture of how gravity acts on large scales. Stars also host planets that may be habitable to life.

The formation of stars begins with a large molecular cloud that becomes unstable to its own gravity, overcoming the resisting internal pressure. The collapse ensues isothermally by radiating away energy until the density reaches a point where the cloud is optically thick, slowing down the collapse as the region halts the release of heat through radiation and becomes more adiabatic. The surface of this dense spherical core is still able to radiate energy, allowing the inside to cool and continue to collapse, while matter outside of the core continues to accrete onto the core. The density within the core continues to grow, eventually getting high enough to start nuclear fusion, which marks the beginning of a protostar. Accretion is eventually halted by the increased radiation pressure that is the result of nuclear fusion and the surrounding dust and gas envelope are blown away, revealing the final product.

The study of star formation is a worthy endeavour, as it seeks to address many questions within astronomy. Star formation affects the observed galactic structure, a structure which is dependent on the galaxy's star formation history. The conditions that govern whether or not star formation will yield low or high mass stars could be dependent on the metallicity or radiation fields of the environment, which may have been different when the universe was younger. Understanding the difference between low and high mass star formation may help elucidate the role of metallicity in star formation.

During the accretion phase of low mass Young Stellar Objects (YSOs) a circumstellar disk forms; in contrast there is little evidence for disks around high mass YSOs. Within a circumstellar disk, the conditions may be possible for planets to form through coagulation. Putting constraints on the physical and chemical conditions responsible for planet formation can narrow down what kind of environment should be considered when searching for planets. The conditions necessary for the formation of life are linked to the conditions necessary for the formation of planets, and so the physics and chemistry of a star forming

environment are connected with the environment that makes the building blocks of life. An investigation into the physical and chemical properties of a star forming environment may assist not only an investigation into the beginning of life, but possibly also where to look for it.

The picture for low-mass (0.02-2 $M_\odot$) star formation is far more developed than that of high-mass star formation. Low mass stars form in larger numbers which means many are found at closer distances and are observable with higher resolution. Their evolution is also easier to follow as there are nearby examples in many stages of evolution. While stars with masses $>50M_\odot$ have been discovered, the theoretical model of single core accretion fails to yield stars with masses $>11M_\odot$, due to fragmentation and radiation pressure from nuclear fusion. An expansion into the understanding of high-mass ($>10M_\odot$) star formation is thus required to complete the picture. An approach to developing this expansion is to look into the conditions under which Intermediate-Mass (IM) (2-10$M_\odot$) stars form.

This thesis encompasses an investigation into the physical and chemical properties of two IM-candidate Young Stellar Objects (YSOs). Molecular line emission of the H_2O molecule in these regions was measured using the Herschel Space Observatory (HSO). Models calculating how radiative transfer proceeds through the molecular envelope surrounding these sources produce emission spectra which are then compared to observed emission spectra. The aim is to use the models and data together to put constraints on physical parameters, such as the size and density of the molecular cloud, as well as chemical properties, including the abundance of H_2O throughout the region.

1.1 Star Formation

Stars are formed in dense regions of interstellar dust and gas. Mass accumulates slowly into a molecular cloud under the forces of gravity, fed by either external stimulation from supernovae or slowly attracting more mass from the leftover material after less violent star deaths. Molecular clouds are gravitationally bound objects that exhibit velocity dispersions on large scales, thermal pressure on smaller scales, and magnetic fields, all of which initially resist further collapse. Star formation begins with these molecular clouds becoming unstable to their own gravity and collapsing against these resisting thermal pressure and magnetic forces (Hartmann, 1998; Hillier, 2008).

The simplest way to approximate when this instability occurs is using virial theorem, which states that a system's time averaged kinetic energy, K, would be equal to half of the potential energy of the force acting upon it, $U/2$ (Carroll & Ostlie, 2007). That is, the cloud would be gravitationally stable if $U + 2K = 0$, where K is the internal kinetic energy and U is the gravitational potential. If the condition where $U + 2K < 0$ were to become true the particles within the system would not have enough kinetic energy to support themselves against the gravitational potential and the system would become unstable to collapse. For example, the system could lose energy due to cooling by the emission of radiation. Beginning with U, we find for a uniform density cloud:

$$U = -\int_0^M \frac{GM(r)dM}{r} \tag{1.1}$$

$$= -\int_0^R \frac{G\left(\frac{4\pi}{3}\rho r^3\right)\left(4\pi r^2 \rho dr\right)}{r} \tag{1.2}$$

$$= -\frac{3}{5}\frac{GM^2}{R} \tag{1.3}$$

and the internal energy K:

$$2K = 3NkT \tag{1.4}$$

$$= \frac{3MkT}{\mu m_H} \tag{1.5}$$

where μm_H is the mass of Hydrogen, and so if collapse occurs when $0 > U + 2K$:

$$0 > U + 2K \tag{1.6}$$

$$\frac{3}{5}\frac{GM^2}{R} > \frac{3MkT}{\mu m_H} \tag{1.7}$$

$$M > \frac{5RkT}{\mu m_H G}, R = \left(\frac{3M}{4\pi\rho_o}\right)^{\frac{1}{3}} \tag{1.8}$$

$$M^2 > \left(\frac{5kT}{\mu m_H G}\right)^3 \left(\frac{3}{4\pi\rho_o}\right) \tag{1.9}$$

$$M > \left(\frac{5kT}{\mu m_H G}\right)^{\frac{3}{2}} \left(\frac{3}{4\pi\rho_o}\right)^{\frac{1}{2}} \tag{1.10}$$

$$M_J = \left(\frac{5kT}{\mu m_H G}\right)^{\frac{3}{2}} \left(\frac{3}{4\pi\rho_o}\right)^{\frac{1}{2}} \tag{1.11}$$

where M_J is known as the Jeans Mass. Once a gas cloud reaches this mass it begins to collapse (Kwok, 2007).

Compared to atoms, molecules have more energy levels available to them due to their high number of rotational transitions that act as an effect cooling mechanism and the cloud continues in a nearly isothermal free-fall collapse. The density will climb until the cloud becomes optically thick to its own cooling radiation shifting the process into an adiabatic phase (Tielens, 2005; Carroll & Ostlie, 2007). This increases the pressure which slows down the infall of material, causing the matter to build up into the first core as it reaches hydrostatic equilibrium. As new material continuously falls onto the expanding core it still radiates in the infrared, and so is cooled upon landing on the core, allowing the release of internal energy from the core, causing it to shrink while gaining mass and rising in temperature.

At around 2000 K, H_2 dissociation slows the rise in temperature until most of the H_2 in the core is dissociated, in which case further gravitational collapse can occur. This central object is what is referred to as a protostar and is the stage of star formation that is the focus of the modelling within this thesis (Stahler & Palla, 2004; Carroll & Ostlie, 2007; Hillier, 2008). While the core begins to

take form, still deeply embedded within a cloud of dust and molecules, matter from the parent cloud is still accreting onto the protostar. The temperature will continue until $\sim 10^6$ K when nuclear fusion begins. At this point, the star will begin producing radiation pressure strong enough to begin dispersing all of the surrounding matter, advancing the once deeply embedded protostar into a visible star (Stahler & Palla, 2004; Carroll & Ostlie, 2007; Hartmann, 1998).

Identifying the stage of evolution from core to star is difficult, as stars form deeply embedded in clouds of dust and gas which absorbs the optical light emitted from the protostar and accretion. This light is, however, re-emitted at much longer wavelengths, leaving the millimeter to infrared wavelength emission key to understanding a YSOs progress through star formation. Studies of the Spectral Energy Distributions (SEDs) [λF_λ vs. λ, See: Section 4] of embedded infrared sources have found four distinct classes of SED shape. In the expression $\lambda F_\lambda \propto \lambda^s$, the spectral index s is evaluated within a range of 2.2 to 10 μm. A Class I object is said to have $s > 0$, showing an SED that rises along the range of wavelength. A star with $-1.5 < s < 0$ would be Class II and considered to be less embedded by a spherical envelope at this stage, but exhibiting a circumstellar disk. Class III stars are those which have $s > -3$, exhibiting no infrared excess from circumstellar dust (Tielens, 2005). The Class 0 classification was developed later and denotes very red sources so deeply embedded that they can only be detected at millimeter and far-infrared wavelengths, and considered to represent an earlier phase of protosteller evolution (Stahler & Palla, 2004; Carroll & Ostlie, 2007).

Rather than in isolation, stars tend to form in clusters. Large molecular clouds with masses much greater than the Jeans mass in equation 1.11 undergo fragmentation, breaking up into several collapsing envelopes which may evolve into star forming or starless clumps of molecular gas and dust.

1.2 The Mass of a Star

This picture of star formation is well established through observations of low-mass (0.02-2$M_\odot$) stars and their YSO candidate equivalents. This is due to the much greater abundance of low mass stars in the sky, and so a higher density of stars results in closer samples that can be studied at higher resolutions. The same cannot be said for high mass (>10$M_\odot$) star formation. Once nuclear fusion begins all infalling material is halted and pushed outwards by radiation pressure, limiting the final mass of a forming star to $\sim$11$M_\odot$ (Stahler & Palla, 2004).

The key to understanding how some of the highest mass (>50$M_\odot$) stars formed is in understanding the environments from which they came. In order to achieve such high stellar masses the mass accretion rate must be several orders of magnitude greater than what is found for the low-mass regime (Stahler & Palla, 2004). This would require higher sound speeds, and thus higher temperatures. Hot cores, regions containing luminous stars, may fulfil this requirement. Densities much higher than that of regions of low-mass star formation, as well as higher turbulent velocities, may also be required for high-mass stars to form through accretion. This may not be enough to circumvent the eventual dispersion of accreting material due to the high luminosity of the outgoing radiation field which can be sufficient to stop accretion and blow the surrounding

cloud away. Another possibility is that high-mass stars are formed in regions so densely crowded that dense cores begin to merge, with protostars already inside collapsing into one another under their own gravity.

While mechanisms that produce high-mass stars have been proposed, their scarcity and greater distances make studying a high-mass star forming regions difficult due to low spatial resolution. Forming deeply embedded in molecular clouds, they quickly disperse any remaining molecular gas and dust away from them, removing the possibility of studying the environment from which they were formed. Observations have shown that high-mass stars do tend to form in centrally located crowded regions of a parent cloud, whereas low-mass stars tend to be dispersed throughout their parent cloud. High turbulent velocities are also observed in regions of suspected high mass star formation, however this may be a result of low resolution, a common issue when studying high-mass stars. Whether or not they are a result of incredibly fast mass accretion or dense core merging is yet to be determined.

In order to better understand the process of high-mass star formation, studies into the formation of Intermediate-Mass (IM) stars (2-10$M_{\odot}$) are performed to bridge the understanding between low and high mass star formation. They form in dense clusters much like high-mass stars but are found at much closer distances to the Sun (<1 kpc) and so can be studied on spatial scales similar to those for low-mass protostars (Fuente *et al.*, 2012). By putting constraints on the physical and chemical properties of the environment in which IM stars are formed a more complete picture of star formation can be developed.

1.3 Molecular Line Emission and Water

Quantum energy levels are the energetic states that particles can occupy. Rather than a continuous spectrum of energy, there are only discrete levels of energy that are possible for an atom or molecule to have at its disposal. Be it the energy of an electron orbiting an atom or molecule, the vibrational energy between the bonds of elements of a molecule, or the rotational energy of a molecule, the transition from one state to the next can occur through collisions with other molecules or interaction with a local radiation field through absorption or emission of a photon. With the energy E_1 of state 1 and E_2 of state 2, the frequency of the photon absorbed or emitted is $\nu = (E_2 - E_1)/h$, where h is Planck's constant, and this frequency is unique to the transition between the first and second state. This work is an examination into the transition between rotational energy states of the water molecule.

Using quantum mechanics, the possible rotational states and their respective energies can be calculated. Excess emission or absorption of photons at these frequencies can be seen in the electromagnetic spectrum as a small increase or decrease in the intensity compared to the background radiation; these rises and dips in intensity are known as molecular lines. The average populations of these levels that the molecules inhabit depend on environmental factors such as temperature, density, and radiation field. In regions of low density, where collisions are not as likely to play a role in energy transition, molecular lines make it possible to study conditions by which they were created, and thus physical and chemical properties of the environment in question.

Since there are more rotational levels available and the energy levels involved

are much lower than that of vibrational or electron orbital levels, molecules are an excellent means of providing the cooling necessary for the collapse of molecular clouds into accreting protostars. Because protostars are deeply embedded in molecular clouds these lines are difficult if not impossible to observe in the optical range of the electromagnetic spectrum. Line emission from rotational transitions tend to lie in the sub-millimeter to infrared regime, making it possible to probe further than the optical depth of the visual spectrum.

CO is the second most abundant molecule in the gas phase after molecular Hydrogen, making it an excellent coolant for a collapsing cloud (Tielens, 2005). It has been useful as a tracer of gas, both in our galaxy as well as others (Stahler & Palla, 2004). It is also useful for estimating the size and mass of a molecular envelope around a star forming region. However, at densities $>10^3$ cm^{-3}, CO starts to become optically thick to its own emission, making it necessary to turn to other molecules to probe more dense regions. In this work, the water molecule, H_2O, is studied as a probe into star forming regions.

The case for water as a probe into star forming region comes from its abundance and how much it varies across warm and cold regions. Oxygen is the most abundant element in the universe after Hydrogen and Helium, with a cosmic abundance relative to H of $\sim 5.6\times10^{-4}$ (Pinsonneault & Delahaye, 2009). If all O is in H_2O then an upper limit on the abundance of H_2O relative to H_2 would be $2\times5.6\times10^{-4}$. Oxygen can, however, be in other forms, such as CO, and the upper limit of the abundance of H_2O is likely to be $\sim10^{-4}$ for temperatures $\sim$100 K and $\sim3\times10^{-4}$ for temperatures $>$250 K. Pure gas-phase chemistry gives a lower limit of the abundance of water of $\sim10^{-7}$, but the effects of water freezing onto dust grains can give a much lower abundance relative to H_2, since H_2 does not freeze out (van Dishoeck *et al.*, 2011).

The formation of H_2O occurs through a number of chemical processes. In cooler regions ($\sim$ 10 K) O and H atoms combine on dust grains to form ice that evaporates around $\sim$ 100 K, while temperatures above 250 K drive gas phase oxygen into water by reactions of O and OH with H (Hillier, 2008; van der Tak *et al.*, 2005). The result is a high variability in abundance of gas-phase water across a large temperature range, making it a unique probe of the environment of a star forming region. The water molecule's sensitivity to the energy deposited in the region around it allows it to be used as a marker of key moments of stellar birth, whether it be the water molecule acting as an effective gas cooler due to its large dipole moment, assisting in the gravitational collapse of gas clouds, or outflow shocks that evaporate water from the dust grains in which they were created (van Dishoeck *et al.*, 2011; van der Tak *et al.*, 2005).

The H_2O molecule is known as an asymmetric top-type molecule, which rotates differently than more simple molecules like CO. The complexity of its rotation allows for many different transitions between rotational states. This complexity is further increased by the fact that there are two configurations of the nuclear spin of the H atoms within the water molecule. The magnetic moments of the protons in the H atoms in the bond could either be aligned, making orthohydrogen, or anti-aligned, giving parahydrogen. These ortho- and para- states result in two sets of rotational states lines (Hillier, 2008). The result is that there are numerous rotational energy levels available to H_2O, seen in Figure 1.1.

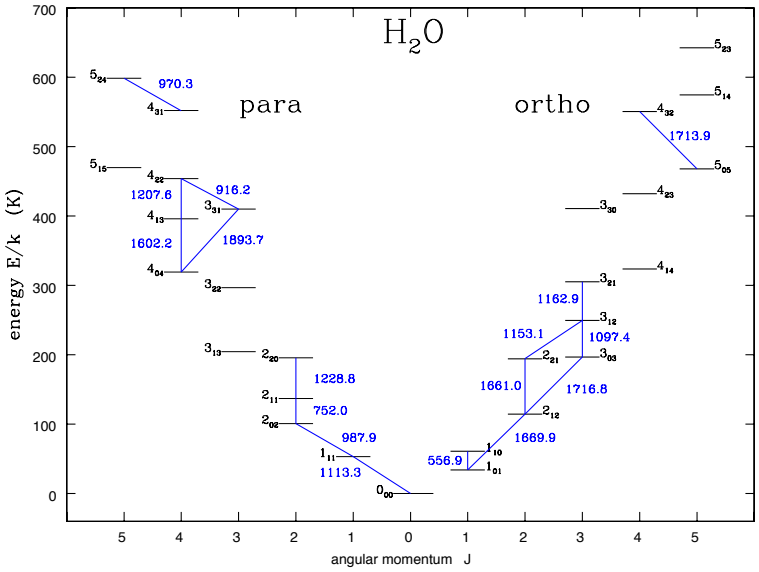

Figure 1.1: Plotted here are the lowest possible rotational energy states available to H_2O. The lines between some of them show transitions that are, in principle, accessible with Heterodyne Instrument for the Far-Infrared (HIFI), with the energy in terms of frequency of the photon released or absorbed. On the left are para-H_2O states and on the right are ortho-H_2O states.

1.4 WISH

Stars form deeply embedded in molecular clouds that are optically thick to the visual spectrum. Observation in the sub-millimeter and infrared regime is crucial in furthering the understanding of star formation, as emission in these wavelengths can assess the physical and chemical properties of a star forming environment.

Emission lines from the rotational transitions in H_2O are particularly useful due to its difference in abundance between warm and cold regions. Varying by orders of magnitude, the abundance of H_2O acts as a measure of energy deposited into molecular clouds. This information can be used to assess different processes within a star forming region, such as gravitational collapse and outflow injection (van Dishoeck *et al.*, 2011).

As mentioned in Section 1.3, there are a large number of rotational energy levels in H_2O. Many of the transitions between them emit lines found at frequencies that are very close to each other. This allows for detailed information about how energy is distributed throughout the system to be gathered from the same region of the electromagnetic spectrum. As measurements of emission spectra made with the Herschel Space Observatory would be spatially unresolved, multiple line observations used in conjunction with radiative transfer analysis are needed to develop an understanding of the physical and chemical processes of the region (van Dishoeck *et al.*, 2011; Hillier, 2008; van der Tak *et al.*, 2005).

The Herschel Space Observatory was launched in May, 2009. With three measurement instruments on board with a spectral range of 55-671 μm its mission is to address a broad range of astronomical inquiry in the sub-mm regime (Pilbratt *et al.*, 2010). Water in Star-forming regions with Herschel (WISH) is a key program of the Herschel Space Observatory, the goal of which is to improve the understanding of what role water has in collapsing envelopes to planet-forming disks (van Dishoeck *et al.*, 2011). Within the WISH team are sub-groups, one of which is the WISH-Intermediate-Mass team. The WISH-IM team is studying 6 IM candidates, 2 of which are studied in this work: Vela IRS 17 and Vela IRS 19. They have been chosen for this work because they have not been well studied; they are in the southern hemisphere and so there is limited ground based data available. These two sources are the same distance from Earth and within the same molecular cloud and so it is useful to make a comparison between these two young stellar objects that are evolving within the same environment. Another of the 6 IM-candidates the WISH-IM team is studying, NGC 7129, has also been presented (Johnstone *et al.*, 2010) but a complete analysis of that object is still under way.

Measurements of H_2O emission lines made with the HIFI (discussed in Section 3.2) are the focus of this work. Radiative transfer across the dust as well as level population of the molecular component are modelled to interpret the measurements and put constraints on environmental parameters.

1.5 Modelling

To model emission spectra of a molecular envelope the processing of stellar radiation through the dusty and molecular envelope must be calculated. The approach begins with the program DUSTY, which solves the radiative transfer

through a spherically symmetric dust cloud, producing a temperature profile of the cloud. Other physical parameters, such as the size, density, and optical depth of the cloud are fitted for with DUSTY modelling. With a model for the basic structure of the envelope, the approach to modelling emission spectra continues with the program RATRAN. Assuming that the ratio of gas to dust is 100:1 and that they share the same temperature profile, RATRAN calculates the radiative transfer through the dusty and molecular envelope using iterative Monte Carlo techniques to calculate the population densities of rotational energy levels; it then uses these population levels to produce emission spectra through ray tracing. The abundance of H_2O relative to H_2 in the inner and outer regions of the molecular cloud and the turbulent velocity are fitted to emission line observations measure with HIFI. Together, DUSTY and RATRAN are used to put constraints on the size and density of the cloud as well as the abundance of H_2O molecules within it.

Figure 1.2 shows a simple drawing of what is being modelled. The drawing depicts a protostar surrounded by an envelope, all of which is within the parent cloud that formed it. Modelling starts with DUSTY, where a dust envelope from r_{inner} to r_{outer} is modelled as described in Chapter 4. With the temperature and density profiles from DUSTY, RATRAN modelling is performed to produce an emission spectra that will be compared with observational data. Radiative transfer through both the dusty and molecular medium is calculated. The abundance of H_2O relative to H_2 set from r_{inner} to the freeze-out radius, which is at T = 90 K for this work, is known as the inner abundance. This is where it is thought that most of the water would be in a gaseous phase (van Dishoeck *et al.*, 2011). The abundance from the freeze-out zone to r_{outer} is the outer abundance, which is set to a much lower value as much less water is expected to be in a gaseous state. In this model motions are assumed to be a random turbulent motion that is constant for each model.

1.6 Outline of the Thesis

The goal of this work is to put constraints on chemical abundances in the envelopes surrounding Intermediate-Mass Young Stellar Object (YSO) candidates. As low-mass and high-mass WISH teams are also doing this research in their respective mass regimes, this work is done to add to the overall picture of water in star forming regions that is being developed. It is thought that all of the water in a star forming region should be in a gaseous state at temperatures above 90 K. Constraints on the inner abundance of H_2O relative to H_2 would be a measurement of the total water in the environment, while constraints on the outer abundance would be a measure of how much H_2O was in the gaseous phase before star formation began. An inner abundance of 10^{-5} and an outer abundance of 10^{-7} would mean $\sim$1% of the water remains in the gaseous phase in cold regions.

This work will also test whether a single power law density distribution and modelled temperature distributions that are a result of this assumption is supported by the data. The density distribution is a result of forces of gravity competing against supporting forces of thermal and turbulent velocities; understanding turbulent velocity within an envelope is critical for understanding supporting forces and therefore the overall dynamics of how fast the cloud is

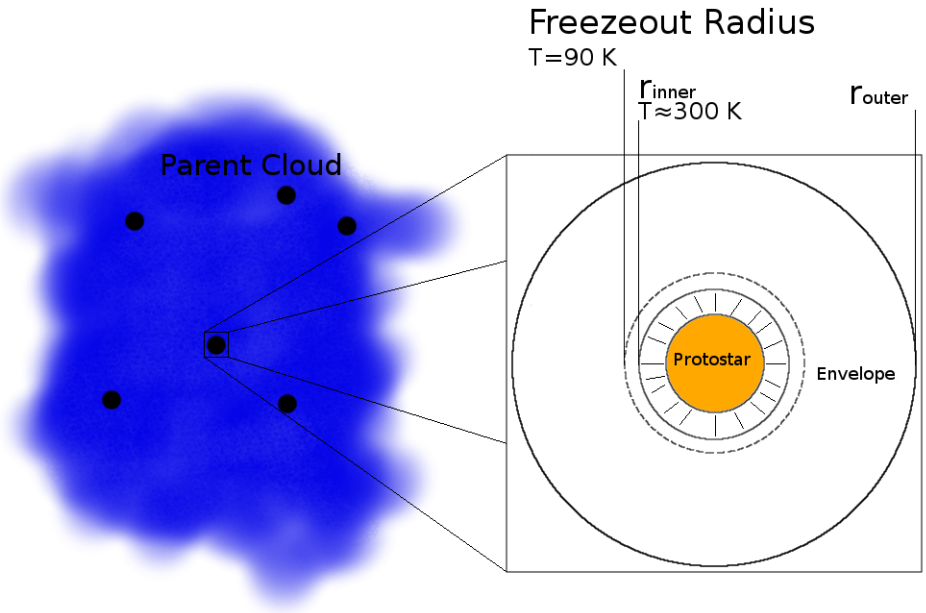

Figure 1.2: Shown here is a simplified drawing of the region being modelled. An envelope surrounds a protostar that is within a greater star forming parent cloud. The inner and outer radii of the envelope are shown. The inner radius is typically ∼50 AU and the outer radius is ∼1000× this value. Also shown is the freeze-out radius for water of 90 K, which is typically ∼10× the inner radius. It should be noted that the protostar size is exaggerated in this picture and would typically be ∼1 AU in size. As well, several objects in the WISH-IM sample exhibit outflows which are not shown in the figure and would larger by a factor of 10 of the outer radius of the envelope.

collapsing. Examining radial velocities are outside the scope of this work.

Chapter 2 is a review of data acquired through previous work that is required for fitting with DUSTY modelling. Chapter 3 details the HIFI instrument aboard the Herschel Space Observatory, observations made using HIFI, and the decomposition of spectra into separate Gaussian components. Chapter 4 describes dust continuum modelling using the DUSTY program as well as the fitting procedures used to constrain physical parameters of the envelope. Chapter 5 continues the line emission modelling procedure with RATRAN. The program takes in the physical parameters of the envelope found through fitting in Chapter 4 to calculate population densities of rotational energy levels in order to produce molecular line emission spectra.

Chapter 2

Review of Previous Data

2.1 The Vela Molecular Ridge and Vela IRS 17 and 19

The first survey that covered the Vela Molecular Ridge (VMR) was the Infrared Astronomical Satellite (IRAS), which was launched with the primary mission of conducting an unbiased survey of the sky in four wavelength bands centred at 12, 25, 60, and 100 μm (Beichman *et al.*, 1988). This was the starting point of research into the Vela Molecular Ridge, a massive molecular cloud system with active regions of star formation. The search for YSOs in the region was first conducted by Liseau et al. (1992) who used the IRAS Point Source Catalogue to find viable candidates for star formation. Having four Giant Molecular Clouds (GMCs) to study, named Vela Molecular Cloud (VMC)-A,B,C, and D, means being able to assess Young Stellar Objects in different regions which share observational and environmental conditions. This particular place in the sky also has an area of equal angular size with no molecular gas right beside it, giving a good, nearby reference field(Massi *et al.*, 1999). It also lies on the galactic plane, where most of the star formation in the galaxy has been found to occur (Liseau *et al.*, 1992; Massi *et al.*, 2007). The VMC-D region shows evidence for recent star formation with no sign of an external triggering mechanism, and star formation proceeding in a relatively quiescent manner (Liseau *et al.*, 1992; Lorenzetti *et al.*, 1993). It is within this region where we find the two YSOs that are the focus of this work.

The IRAS Point Source Catalogue Version 2 was used by Liseau *et al.* (1992) in the beginning of what would become a series of studies into star formation in the Vela Molecular Ridge (Beichman *et al.*, 1988; Liseau *et al.*, 1992). Of the 8000 point sources in this IRAS sample, found 229 that met their criteria for selection of Class 1 objects. These criteria were that the flux densities in the first 3 IRAS bands were valid detections, the IRAS colour be red, and the source not an infrared galaxy. These sources were then observed with the ESO 1 meter telescope at La Silla, Chile, in the J(1.2μm), H(1.6μm), K(2.2μm), L(3.8μm), and M(4.6μm) bands (Liseau *et al.*, 1992). Vela IRS 17 and 19 were amongst those that fit these criteria. They are both located within the VMR-cloud D. Vela IRS 17, also known as IRAS 08448-4343, is a Class 1 Young Stellar Object which is part of a filament of mm sources. Deeply embedded

but illuminated by a reflection nebula, it has been shown that Vela IRS 17 can be further decomposed into two embedded cores (Massi *et al.*, 2007; Giannini *et al.*, 2005; Massi *et al.*, 1999; McCoey *et al.*, 2013). Vela IRS 19, also known as IRAS 08470-4321, is also a Class 1 source more deeply embedded than Vela IRS 17 that is also illuminated by a reflection nebula (McCoey *et al.*, 2013). It is another source of interest, particularly because of its similarities to Vela IRS 17.

As will be shown next, these are two very similar YSOs, yet, as will be shown later, have very different properties when their spectra are compared against one another. These are 2 of the 6 IM candidates for the WISH-IM team (van Dishoeck *et al.*, 2011).

2.2 Properties necessary for modelling

In order to produce the temperature and density profiles needed for RATRAN modelling, the DUSTY program is used. The distance to the source, luminosity, dust envelope edge, single power-law density parameter α, and optical depth at some wavelength τ are needed as inputs for DUSTY to produce the temperature and density profiles (See: Chapter 4). These DUSTY inputs come from ground-based observation.

The distance to the cloud was estimated by Liseau *et al.* (1992) using two methods. The first was using IR photometry to identify the spectral type of the sources and then calculating their photometric distances. IRS 11 and IRS 16 were calculated to a distance of 740 pc and 1200 pc, respectively, which gave the lower and upper limits of the distance to VMC-D. The second was using the empirical relationship for cloud distances developed by Herbst & Sawyer (1981) and was found to be 700 $\pm$ 200 pc for VMC-D. The latter has been the most commonly accepted value and will be what is used for this thesis (Giannini *et al.*, 2005; Elia *et al.*, 2007; Massi *et al.*, 2007).

The source luminosities were first estimated by Liseau et al. (1992) who found $L_{17} = 670L_{\odot}$ for Vela IRS 17 and $L_{19} = 776L_{\odot}$ for Vela IRS 19 (Liseau *et al.*, 1992). This was done by first identifying the sources within the IRAS catalogue, then making J, H, K, L, and M measurements on any source with K $\leq 12^m$, and integrating within these points (Liseau *et al.*, 1992). Later higher resolution imaging in the K band went on to show evidence of clustering within both of these sources drove an investigation into Vela IRS 17 to determine the true source of an observed jet as well as a more accurate measure of the luminosity (Massi *et al.*, 1999). The main source, labelled as NIR #57, had its contribution to luminosity distinguished from the other NIR sources in the region and was found to be $715L_{\odot}$ by integrating from 1.6μm to 1.2 mm; this is adopted as the source luminosity for the Vela IRS 17 source here (Massi *et al.*, 1999; Giannini *et al.*, 2005). The most prominent jet was found to be driven by NIR #40 but other jets in the region have been associated with other NIR clusters, NIR #57 being one of them (Giannini *et al.*, 2005).

The other three parameters required by DUSTY: envelope edge, α, and τ, are to be chosen through fitting. For reasons that will be made clear in Chapter 4, we require fitting to continuum images and fluxes at various wavelengths. In this work both a 1.2 mm continuum image and continuum fluxes measured through the infrared and sub-millimeter are used. The continuum image is used

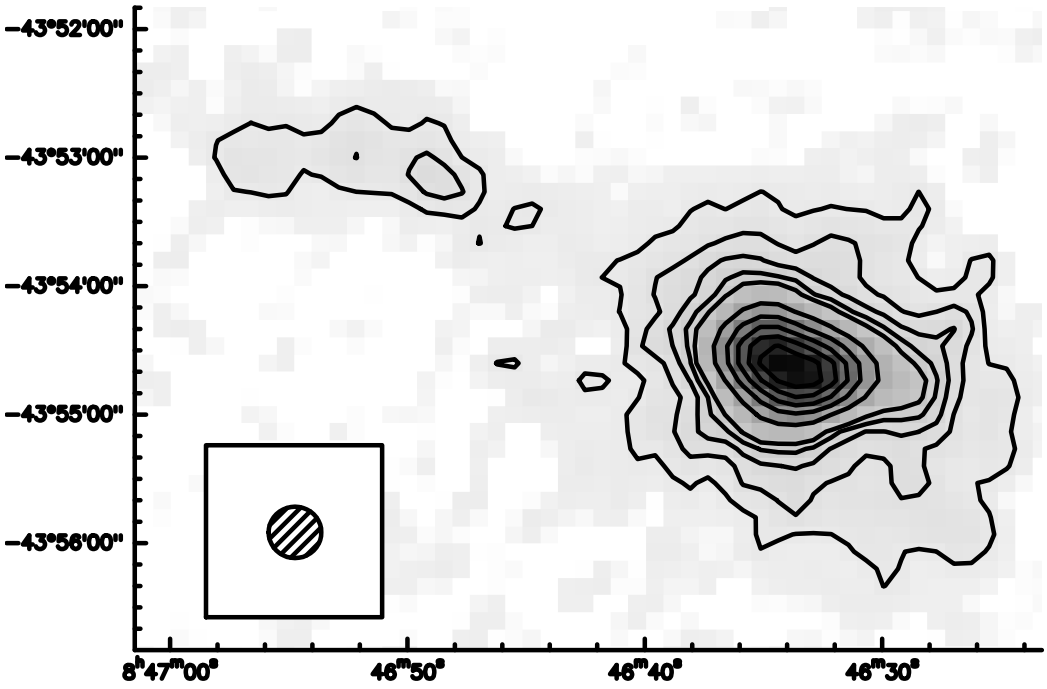

Figure 2.1: 1.2 mm continuum map for Vela IRS 17 (From Massi *et al.* (2007))

to get the variation of surface brightness from the centre of the source to the outer edges while the fluxes are used to produce a Spectral Energy Density (SED).

To get the surface brightness profile needed for the fitting procedure a 1.2mm continuum map of the area produced by Massi et al. 2007 was used. This area of the D cloud of the Vela molecular ridge was observed using the the 37-channel bolometer array SIMBA at the Swedish-ESO SUbmillimeter Telescope site in La Silla, Chile. They calculated the noise to be ∼20mJy/beam and calculated their flux calibration to be accurate within ∼20% and the Half-Power Beam Width is measured to be 24″ (Massi *et al.*, 2007; Nyman *et al.*, 2001). The maps of the sources studied in this work are in Figures 2.1 and 2.2. In order to extract a surface brightness profile from the data, data from each map were split into annuli in increments of 8″ from the centre of the source with a 4″ window on each side. The mean of each annulus was taken to be the value at that distance from the source and the error of the mean was calculated from the scatter from the mean at each respective annulus.

Surface Brightness profile fitting on its own cannot constrain τ (Jørgensen, 2004). In order to get a fit for τ the SED output from DUSTY is compared with flux data measured at wavelengths in previous studies. As mentioned earlier, Liseau et al. 1992 made an estimate for the luminosities of Vela IRS 17 and IRS 19 using, in part, IRAS data. Not every IRAS band is useful, however, as shorter wavelengths have emission from material not modelled by DUSTY, such as small dust grains and PAH bands (Olmi *et al.*, 2009). For the purposes of this paper, flux measurements for wavelengths $< 60\mu$m were omitted. Only

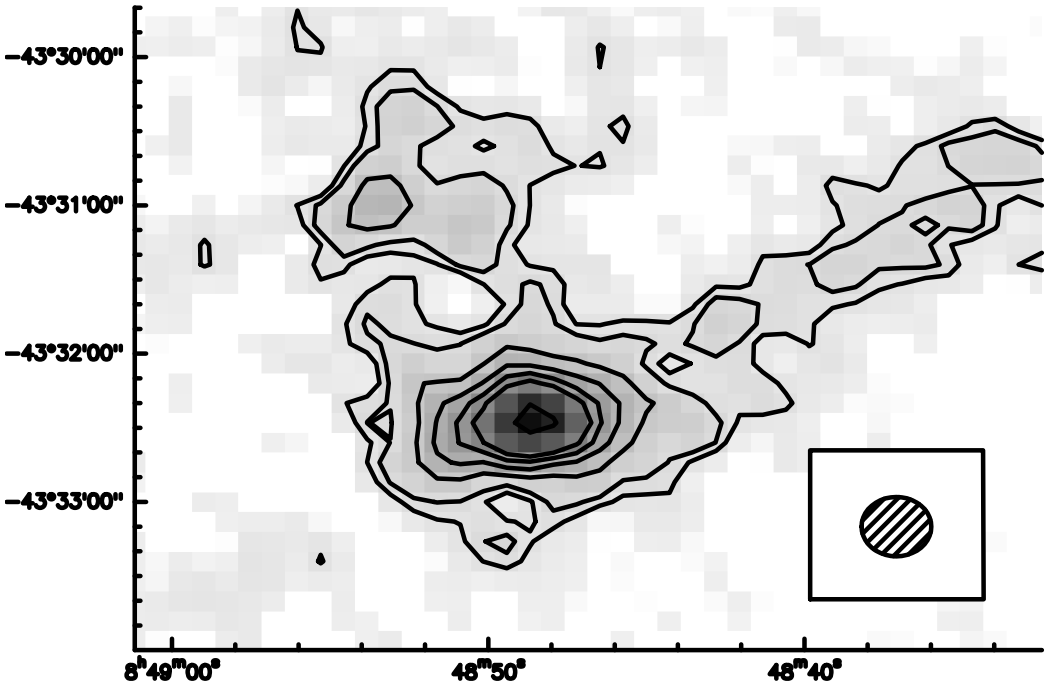

Figure 2.2: 1.2 mm continuum map for Vela IRS 19 (From Massi *et al.* (2007))

the 60 and 100 μm IRAS bands could be used. For more data in the sub-mm range, the BLAST survey proved useful.

The Balloon-borne Large-Aperture Submillimeter Telescope (BLAST) carried out two long duration flights, one of which mapped out $\sim 60^\circ \times 60^\circ$ of the Vela Molecular Cloud with its three-band photometry, each centred around the 250μm, 350μm, and 500μm wavelengths (Olmi *et al.*, 2009). These bands are quite useful, as they are near, if not at the peak of the SEDs. It is these three BLAST and the two previously mentioned IRAS points that are used in fitting DUSTY models to SEDs in order to constrain τ. The SEDs are plotted in Figures 4.3 and 4.4.

Although not specifically used as an input parameter nor fitted to, it is useful to compare the the estimated masses of the sources with the mass of the envelope of the best-fit model to see if the chosen fit is sensible. Massi et al. (1999) made an estimate of the masses of both sources using 1.3 mm observations by using the formula:

$$F_\nu = \frac{j_\nu \left(\frac{4\pi}{3}R^3\right)}{D^2}, j_\nu = \kappa_\nu B_\nu(T_d) \tag{2.1}$$

$$F_\nu = \frac{\kappa_\nu \cdot B_\nu(T_d)}{D^2}\left(\frac{4\pi}{3}R^3\right) \tag{2.2}$$

$$F_\nu = \frac{\kappa_\nu \cdot B_\nu(T_d)}{D^2}\left(\frac{M_d}{\rho_d}\right) \tag{2.3}$$

$$M_d = \frac{F_\nu \cdot D^2}{\kappa_\nu \cdot B_\nu(T_d)} \tag{2.4}$$

where F_ν is the measured flux density, D is the distance to the source, $B_\nu(T_d)$ is the Planck Function, κ_ν is the opacity per unit gas mass, and we assume the dust density $\rho_d = 1$ g m^{-3}(Massi *et al.*, 1999). Mass estimates from using flux data are particularly sensitive to the choice of κ_ν as it is a measure of the extinction of light through a medium. Using $\kappa_\nu \sim 1$ cm^2 g^{-1}, and assuming T_d = 30 K, the masses for Vela IRS 17 and Vela IRS 19 were valued at 6.4 M$_\odot$ and 3.5 M$_\odot$, respectively (Massi *et al.*, 1999). These numbers were later adjusted in Massi et al. 2007, using the SIMBA array at SEST, as well as $\kappa_\nu = 0.5$ cm^2 g^{-1}, and they found masses of 88 M$_\odot$ and 18 M$_\odot$, respectively (Massi *et al.*, 2007).

Work done since then with the BLAST survey has shown similar results. Assuming an optically thin emission from an isothermal modified blackbody, the following equation,

$$S_\nu = A \left(\frac{\nu}{\nu_0} \right)^\beta B_\nu(T)$$

where

$$A = \frac{M_g \kappa_0}{100 \times d^2}$$

is used to estimate the mass. With β chosen to be 2, $\kappa_\nu = 16$ cm^2 g^{-1} evaluated at $\nu_0 = c/250$ μm, S_ν is fitted to all of BLAST's data as well as archived photometry using χ^2 optimization (See: 4), leaving only A and T to vary. The masses were estimated with this method to be 98.0 $\pm$ 10.6 M$_\odot$ and 16.5 $\pm$ 2.3 $M_\odot$ for Vela IRS 17 and Vela IRS 19, respectively (Olmi *et al.*, 2009). This also gave temperature T as 18.0 $\pm$ 0.3 K and 20.7 $\pm$ 0.4 K, respectively.

The surface brightness profile and SED data will be used with DUSTY modelling and reducedχ^2 fitting to constrain the size, density, and optical depth of the dust in the envelope surrounding Vela IRS 17 and Vela IRS 19. The program RATRAN will then use these details of the environment to model water emission lines that, along with observational data from the Herschel Space Observatory, will help to put more constraints on the physical and chemical properties of the molecular envelope.

Chapter 3

Molecular Spectroscopy and the Herschel Space Observatory

3.1 Introduction

As mentioned in the introduction, the study of molecular emission lines is very useful in the investigation of star formation. Stars are formed deeply embedded in dense molecular clouds that are opaque to the visual range of the electromagnetic spectrum. Any radiation emitted from a stellar source is absorbed and re-emitted at longer wavelengths by the dust and molecules in the surrounding envelope. Molecular emission in particular is a useful tracer of kinematics and chemical abundance, which in turn is useful for detection of stellar properties which are indicative of different stages of stellar evolution. Water in particular is a useful tracer, as its abundance in the gas state is suspected to vary by up to three orders of magnitude between warm and cold regions (van Dishoeck *et al.*, 2011). It is also able to probe deeper than the more abundant CO tracer, which becomes optically thick at higher densities as molecular cloud collapses.

3.2 Observations with Herschel

The Herschel Space Observatory, launched in May 2009, is a spacecraft that offers a never-before attained level of observation ability in the sub-millimeter and far infrared spectrum (Pilbratt *et al.*, 2010). With a telescope 3 meters in size, it is the biggest telescope ever launched, with three instruments on board that compliment each other to provide extensive imaging ability within its 55 μm - 671 μm range. The main objectives of Herschel span over a broad range, from star formation and its interaction with the ISM in our galaxy, to cosmology and galaxy evolution studied by looking far into space and time.

The Heterodyne Instrument for the Far Infrared (HIFI) measures at very high spectral resolution over a wavelength range of 480-1250 GHz and 1410-1910 GHz. The main scientific motivation for using HIFI is to develop a better understanding of the relationship between stars and the ISM (de Graauw *et al.*,

Table 3.1: Breakdown of observations of Vela IRS 17 made with HIFI

Transition	Rest frequency (GHz)	band	Integration (s)	OD/date (dd-mm-yy)
o-H_2O 1_{10} –1_{01}	556.936	1a	629	568/03-12-10
p-H_2O 1_{11} –0_{00}	1113.343	4b	2222	391/09-06-10
p-H_2O 2_{02} –1_{11}	987.927	4a	1025	391/08-06-10
p-H_2O 2_{11} –2_{02}	752.033	2b	721	429/17-07-10
o-H_2O 3_{12} –2_{21}	1153.127	5a	598	398/15-06-10

2010). In particular, HIFI has been optimized for water lines emitted from rotational transitions ending the ground state that are crucial for cold water absorption studies. As part of a guaranteed time key programme on Herschel, Water In Star-forming regions with Herschel (WISH) had HIFI make observations of the Vela IRS 17 and Vela IRS 19 sources to measure water line spectra in the regions. The goal is to use these observations to help put constraints on the physical and chemical characteristics of the star forming region, in an attempt to further our understanding of star-formation, particularly in the intermediate-mass region, as well as the role water plays in this process (van Dishoeck *et al.*, 2011; de Graauw *et al.*, 2010; in the ESA, 2011).

Single point observations with three different reference schemes were performed on the two sources of interest. Each reference scheme employs a different method to account for and subtract baseline emission from the region of interest. In general, the simplest method is to point the telescope to a nearby position 2 degrees away from the target that is absent of emission, called the OFF position, and take a measurement that is to be subtracted from the ON position. A reference scheme known as Dual Beam Switch acts similarly, except that it uses an internal mirror to adjust the beam path to reference a region 3 arc minutes from the target. This method provides better baseline removal; however the moving of the internal mirror slightly adjusts the path of incoming light from the target which has the potential of creating residual standing waves. To account for this, the satellite's position is adjusted such that the OFF position with regard to the internal mirror position is now on the target, while the ON position becomes the new reference point. This removes standing waves to a first order. This scheme was used for the measurements of all non-ground state lines.

Another reference scheme, known as Frequency Switch, measures the target as usual, then 'throws' the frequency of the Local Oscillator (LO) by a small amount set by the user to make the measurement again. The difference between the two spectra effectively removes the baseline. In a region of extended emission, where a 3 arc minute deflection of the inner mirror fails to provide a clean reference field, the Frequency Switch reference scheme provides a useful way to make efficient measurements of relatively simple spectra. As this is seems to be the case for the extent of the CO 1-0 protosteller envelopes, observations of the $H_2^{18}O$ $1_{10} - 0_{01}$ (547 GHz) transition line were done using the Frequency Switch with a sky reference scheme (McCoey *et al.*, 2013).

Finally, the Load Chop reference scheme can be used in situations where the region of interest has no emission-free zones that can be used in any Position Switch or Dual Beam Switch, or if the source is too spectrally complex for Frequency Switch. The Load Chop scheme uses internal cold loads as a reference

Table 3.2: Breakdown of observations of Vela IRS 19 made with HIFI

Transition	Rest frequency (GHz)	band	Integration (s)	OD/date (dd-mm-yy)
o-H_2O 1_{10} –1_{01}	556.936	1a	405	397/15-06-10
o-H_2O 1_{10} –1_{01}	556.936	1a	629	568/03-12-10
p-H_2O 1_{11} –0_{00}	1113.343	4b	2222	391/09-06-10
p-H_2O 2_{02} –1_{11}	987.927	4a	1025	391/08-06-10
p-H_2O 2_{11} –2_{02}	752.033	2b	721	429/17-07-10
o-H_2O 3_{12} –2_{21}	1153.127	5a	598	398/15-06-10

to calibrate for short term changes within the HIFI instrumentation. It is with this observation scheme that measurements of the $H_2^{18}O$ $1_{10} - 0_{01}$ (547 GHz) and $H_2^{18}O$ $1_{10} - 0_{01}$ (547 GHz) lines were made. All three methods used a sky reference in the OFF position to relieve any standing wave effects expected with this observation modes (McCoey *et al.*, 2013; de Graauw *et al.*, 2010; in the ESA, 2011).

After any of the three observing modes, one of two spectrometers can be used to provide the file output spectra. The Intermediate Frequency, which is produced after mixing the incoming radiation with the Local Oscillator of the machine using any of the three observation modes, is sent to either the Wide Band Spectrometer (WBS) or the High Resolution Spectrometer (HRS). The WBS uses an Acousto-Optical Spectrometer to first separate the 4 GHZ IF signal to four 1 GHz samples to be further processed by 4 CCD photodiodes, resulting in a resolution of 1.1 MHz (in the ESA, 2011). The HRS is an Auto-Correlator Spectrometer (ACS) that provides 4 modes of operation that offer resolutions spanning from 0.125-1.0 MHz. This entire process is performed for both horizontal and vertical polarizations.

3.3 Data Reduction

The data were initially reprocessed using the pipeline in HIPE 7.1 and the calibration version HIFI_CAL_6_0 (McCoey *et al.*, 2013). Subsequent data reduction used HIPE 8.1. Temperatures were converted from antenna temperature using methods described in a note released on the HIFI calibration website (Olberg, 2010). Second-order polynomial baselines were removed from each sub-band of the WBS; higher orders were required in cases where spurs appeared in the baseline. The sub-bands within the HRS data were more narrow than the broad lines of interest, and so no baseline removal was attempted; the HRS data were used to verify features seen in the WBS spectra. The horizontal and vertical polarizations are averaged together. Tables 3.1 and 3.2 list the H_2O transition lines observed with HIFI that will be used in this work. These lines were selected as they were predicted to be bright from models before the launch of Herschel and are also the same lines used as low and high mass WISH teams (Hillier, 2008).

Up to three Gaussian profiles were used in an attempt to break down the line profiles into separate components: 'broad', 'medium', and 'narrow'. This classification denoted by having a FWHM $>$ 20 km s^{-1}, 5-20 km s^{-1}, and $<$ 5 km s^{-1}, respectively (McCoey *et al.*, 2013). Fitting was done with the

Table 3.3: Parameters of various Gaussian components fitted to spectra for Vela IRS 17

Line (GHz)	rms^1 (mK)	Component	ν_0 (km s^{-1})	Flux (K)	δv_{FWHM} (km s^{-1})	$\int$ T dv (K km s^{-1})
557	19	Broad	8.0	0.168	22.7	4.07
		Medium	4.5	0.853	7.3	6.62
		Narrow	3.7	-0.545	3.25	-1.89
1113	34	Broad	8.0	0.284	24.2	7.32
		P-Cygni (Medium)	4.5	1.69	5.77	10.4
		P-Cygni (Narrow)	4.2	-1.94	4.91	-10.1
752	22	Broad	8.0	0.142	22.1	3.33
		Medium	4.5	0.452	4.05	1.95
		Narrow	-	-	-	
987	21	Broad	8.0	0.266	27.7	7.83
		Medium	4.5	0.508	4.80	2.6
		Narrow	-	-	-	-
1153	95	Broad	-	-		
		Medium	8.0	0.174	10.5	1.94
		Narrow	-	-	-	

Table 3.4: Parameters of various Gaussian components fitted to spectra for Vela IRS 19

Line (GHz)	rms^1 (mK)	Component	ν_0 (km s^{-1})	Flux (K)	δv_{FWHM} (km s^{-1})	$\int$ T dv (K km s^{-1})
557	26	Broad	14.0	0.149	27.3	4.32
		Medium	7.0	-0.131	11.8	-1.64
		Narrow	-	-	-	
1113	34	Broad	14.0	0.140	36.1	5.36
		Medium	7.8	-0.174	10.1	-1.87
		Narrow	12.2	0.186	0.77	0.153
752	20	Broad	14.0	0.0532	33.5	0.482
		Medium	11.5	0.116	5.66	0.228
		Narrow	12.2	0.0721	1.41	0.0941
987	20	Broad	14.0	0.149	35.6	0.453
		Medium	12.1	0.146	4.44	0.654
		Narrow	12.2	0.0697	1.88	0.363
1153	97	Broad	14.0	0.136	40.1	5.82
		Medium	-	-	-	
		Narrow	-	-	-	

SpectrumFitter routine within HIPE that automatically produces the Gaussians with the minimum χ^2 for the total fit, total fit meaning the sum of all the Gaussians. Tables 3.3 and 3.4 give the parameters of the Gaussian profiles fitted as either component, while Figures 3.1 and 3.2 are the line profiles with their Gaussian component fits.

3.4 Discussion

Decomposing emission line profiles into several Gaussian components makes it possible to assess different physical components of the YSO. The broad component (> 20 km s^{-1}) is associated with high velocity outflow from the protostar, with emission originating from shocks along cavity walls. The narrow component (< 5 km s^{-1}) is thought to arise from a heated envelope that has far less turbulence within it. The medium component is thought to be a result of turbulent interaction between the outflow and inner envelope, possibly through shocks on smaller spatial scales than the outflow or UV heating. If the outflow is not tangential to the line-of-sight, a map of these components would show red and blue shifted regions offset from the source and likely on opposite sides of each other. When examining turbulent velocity ranges similar to those that define narrow, medium, and broad components, the red and blue shifted regions would appear to increase in distance from the source (Lada & Fich, 1996).

Vela IRS 17 H_2O emission lines observed with HIFI are displayed in Figure 3.1. Of the lines plotted, the strongest is the 557 GHz line followed by 987 GHz, and 752 GHz. All observed lines exhibit emission line broadening, while the 557 GHz and 1113 GHz lines both show some absorption at the centre of their lines. The 1113 GHz exhibits a P-Cygni profile. When the spectra are decomposed into Gaussian components it can be seen that all observed lines exhibit broad, and with the exception of 1153 GHz, medium components. 557 GHz and 1113 GHz lines both also have narrow components. The broad components of all observed lines are offset from the local standard of rest, which is $v_{lsr} = 3.9$ km s^{-1} (McCoey *et al.*, 2013), with their peaks at 8.0 km s^{-1} and have FWHMs of ≈ 25 km s^{-1} . The medium components peak at 4.5 km s^{-1} with FWHM values of ≈ 5 km s^{-1}, with the exception of the 557 GHz line which has a medium component FWHM of 7.3 km s^{-1}.

Vela IRS 19 H_2O emission lines observed with HIFI are displayed in Figure 3.2. These lines are noticeably weaker than those of Vela IRS 17. Of the lines plotted, the strongest is the 987 GHz line followed by 752 GHz, and 1113 GHz. After the spectra are decomposed, it can be shown that all emission lines observed have broad components, and with the exception of 1153 GHz, medium components. A narrow component can be found in 1113 GHz, 987 GHz, and 752 GHz emission lines. The local standard of rest for Vela IRS 19 is measured to be $v_{lsr} = 12.2$ km s^{-1} (McCoey *et al.*, 2013). The broad components peak at 14.0 km s^{-1}, and the medium components for the 1113 GHz and 557 GHz lines peak at 7.8 and 7.0 km s^{-1}, respectively. The medium components for 752 GHz and 987 GHz peak at 11.5 km s^{-1} and 12.1 km s^{-1}.

Overall, observed emission lines from Vela IRS 19 appear to be much weaker than those observed for Vela IRS 17. As the IM-YSO candidates are forming in the same molecular cloud, it would be useful to study what it is about their environments that lead to such different observed emission.

The separation of water emission lines into Gaussian components has been used to put constraints on physical components of star forming regions of low and intermediate-mass candidate YSOs (Kristensen *et al.*, 2010; Johnstone *et al.*, 2010; McCoey *et al.*, 2013). Since each component is thought to originate from different parts of the protostellar envelope, RATRAN will be used to attempt to reproduce the Gaussian profiles in Figures 3.1 and 3.2 separately in an effort to put constraints on turbulent velocity and inner and outer abundances of water relative to H_2.

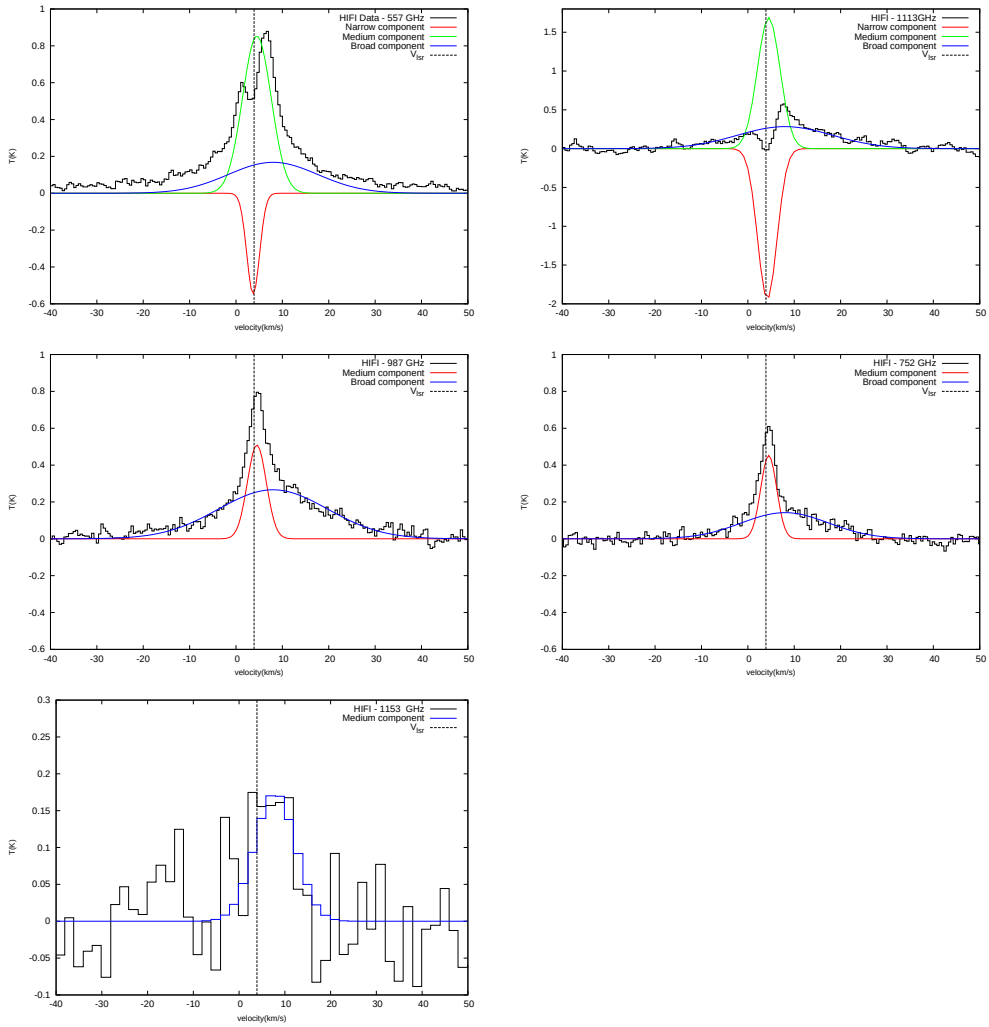

Figure 3.1: Vela IRS 17 spectra of various lines. Their respective components are broken down in Table 3.3.

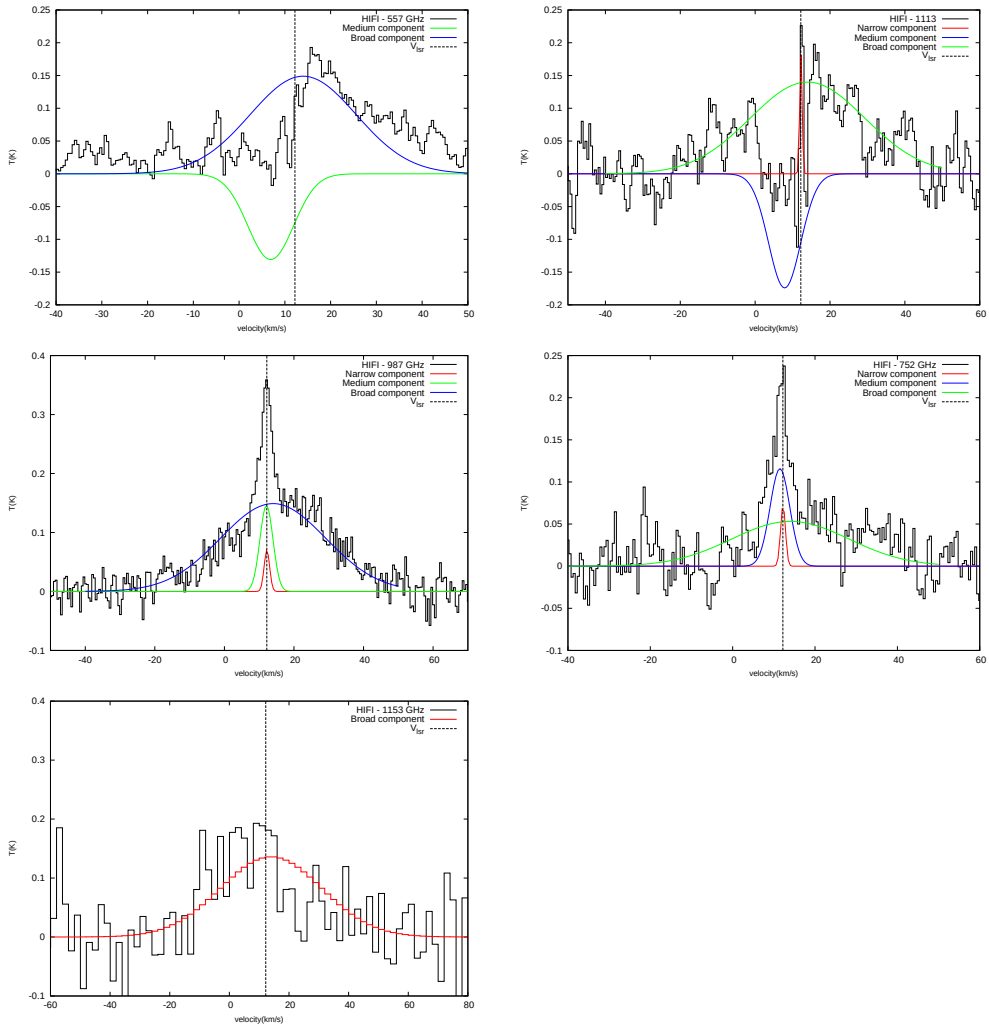

Figure 3.2: Vela IRS 19 spectra of various lines. Their respective components are broken down in Table 3.4

Chapter 4

Dust Continuum Modelling

As will be detailed in Chapter 5, RATRAN requires the density and temperature profile of the dust within envelope, as well as the envelope size and τ_{100}, the optical depth at frequency ν=100μm. For this, the 1D radiative transfer modelling program DUSTY,version 2.06, is used. DUSTY was developed by Ivezic *et al.* (1999) to calculate how a dusty region of the ISM processes radiation from some source. The program calculates the radiative transfer through a dusty environment for either spherical or planar geometries, the former being what is used in this study.

Using the luminosity of the stellar source, dust envelope's size, density, and opacity, DUSTY is used to produce the density and temperature profile of the envelopes surrounding Vela IRS 17 and Vela IRS 19. In order to adopt the correct input parameters, fitting to data detailed in Chapter 2 is required.

4.1 Fitting parameters

A simplified expression of radiative transfer in equation form is as follows:

$$I_\nu(r) = I_\nu(r_0)\exp^{-\tau_\nu(r_0,r)} \tag{4.1}$$

where

$$\delta\tau_\nu = \rho(r')\kappa_\nu\delta r' \tag{4.2}$$

$$\tau_\nu = \rho_0\kappa_\nu\int_{r_i}^{r_o} {r'}^{-\alpha}\delta r' \tag{4.3}$$

where $I_\nu(r_0)$ is the initial intensity of the radiation, $I_\nu(r)$ is the resultant intensity, and a single power law density distribution is assumed. Of the inputs required for DUSTY, four can be seen in equation 4.3; these are the optical depth τ_{100}, power law of the density distribution α, and the inner and outer radii, r_i and r_o, respectively. Other inputs include the Interstellar Radiation Field (ISRF) the external radiation field outside of the cloud, which is assumed to look like diminished starlight (Black, 1994) as well as dust opacities from Ossenkopf & Henning (1994), which were calculated using a standard MNR (Mathis *et al.*, 1977) distribution for the diffuse ISM with thin ice mantles and

a gas density of $n = 10^6 \mathrm{cm}^{-3}$, evolved after 10^5 years of coagulation. The source luminosity L_* and inner radius of the dust envelope r_{in} are two of source specific input parameters, the latter of which is constrained by assuming the inner temperature of the dust region is T =300 K, the temperature at which most of the dust is destroyed. By using the observed luminosity(L_*) of the sources we can find r_{in} with the Stefan-Boltzmann equation:

$$r_{in}^2 = \frac{L}{4\pi\sigma T^4}$$

The input parameter Y is the relative thickness of the envelope, that is, $Y = r_{out}/r_{in}$, where the outer boundary of the envelope is r_{out}. Assuming a single power law density, α in $\rho \propto r^{-\alpha}$ is another of the parameters needed for a DUSTY model. The single-power law is adopted as it's commonly used by theorists for free falling envelopes as well as isothermal spheres with no external pressure, both of which have $\alpha = 1.5$ (Crimier *et al.*, 2010). The final parameter needed is the optical depth at $100\mu m$, τ_{100} (Ivezic *et al.*, 1999; Jørgensen, 2004). With L_* and r_{in} constrained by the results of previous work this leaves α, Y, and τ_{100} to be determined through fitting, where the best fit is used to produce the temperature and density profiles needed for the RATRAN code.

4.2 Modelling Approach

To find the best-fit DUSTY model a method similar to that used by others is implemented, whereby α and Y are found by fitting the DUSTY surface brightness output to continuum data and τ_{100} is found by fitting the DUSTY SED output to known flux data (Jørgensen, 2004; Crimier *et al.*, 2010). Models were run in the ranges $\alpha = 1.0 - 1.9$, and $\tau_{100} = 0.1 - 1.5$ in steps of 0.1. The range for α was chosen to centre around a commonly used value of 1.5, which is that of an isothermal sphere, while the range for τ_{100} was chosen to cover the range from an optically thin to an optically thick envelope. For Vela IRS 17 and Vela IRS 19 specifically, the range for Y was chosen to centre around the Y value corresponding to the furthest data point from the centre of the continuum maps in Figures 2.1 and 2.2 that had a signal-to-noise ratio >3. The range was chosen to be $\pm \sim 600$ this value, and extended if necessary. For Vela IRS 17 this was $Y = 550 - 1750$, and for Vela IRS 17 this was $Y = 100 - 1650$, in steps of 25 and 50 respectively.

The method of finding the best-fit with DUSTY first involves finding α and Y by determining the best fit between the surface brightness profiles of the models and the observed surface brightness data. τ_{100} cannot be constrained using Surface Brightness profile data, as τ_{100} is a measure of light extinction from only the centre of the source, and so the choice for τ_{100} at this point would be relatively arbitrary. This is effectively shown in the middle plot of Figure 4.1, where any choice of τ_{100} in this range would result in the same α. Then, using the best-fit α and Y, the best fit between modelled SEDs and available flux data are found to determine a value for τ_{100}. This is then repeated, with the choice of τ_{100} no longer being arbitrary and instead held constant as α and Y are again fitted for. With these new values for α and Y, τ_{100} is once again fitted for. A third iteration is performed to check for convergence.

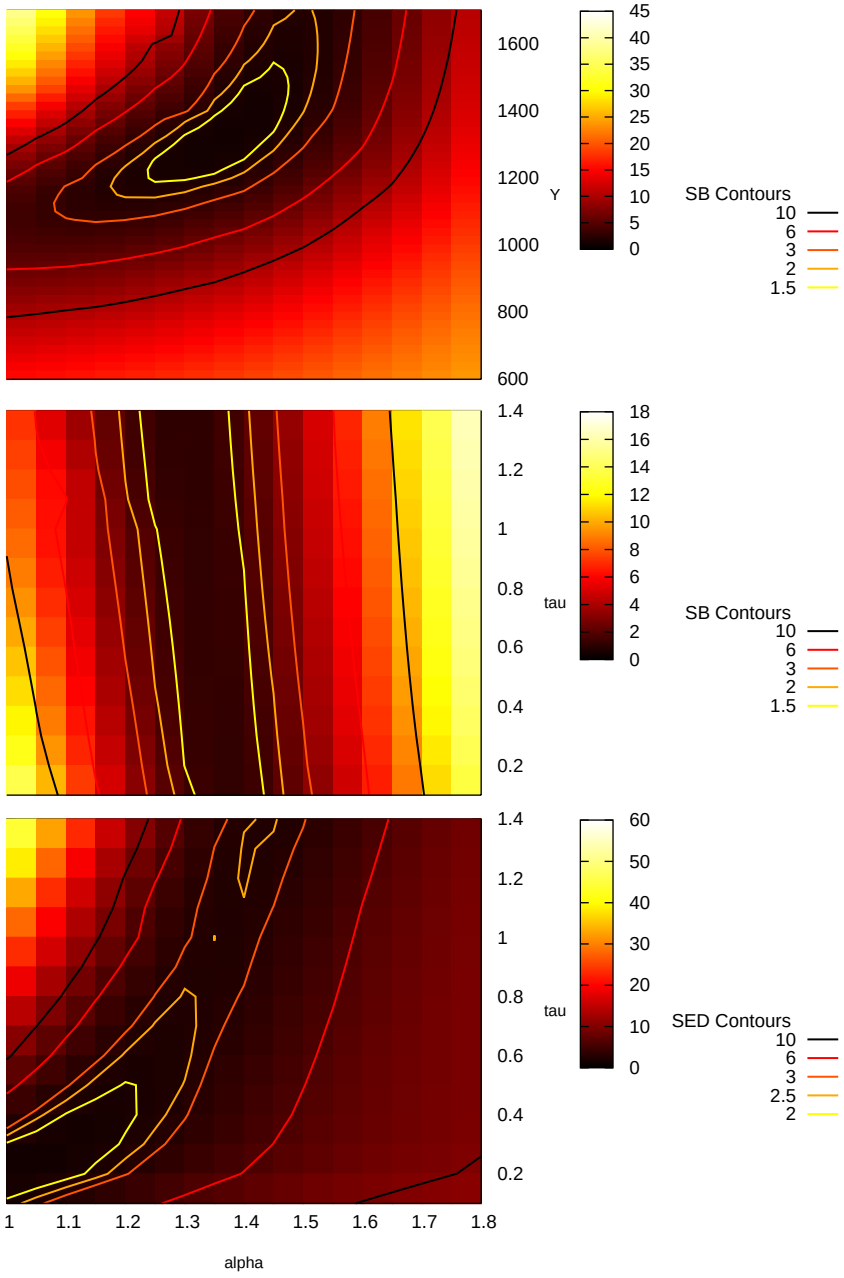

Figure 4.1: Vela IRS 17 Contour plot of χ^2_{SB} (*Top*: $\alpha - Y$ plane, *Middle*: $\alpha - \tau$ plane) and χ^2_{SED} (*Bottom*: $\alpha - \tau$ plane), divided by their respective lowest χ^2_{red}. Contour lines are multiples of the lowest χ^2_{red} of the plane. χ^2_{red} values can be found in Table 4.1

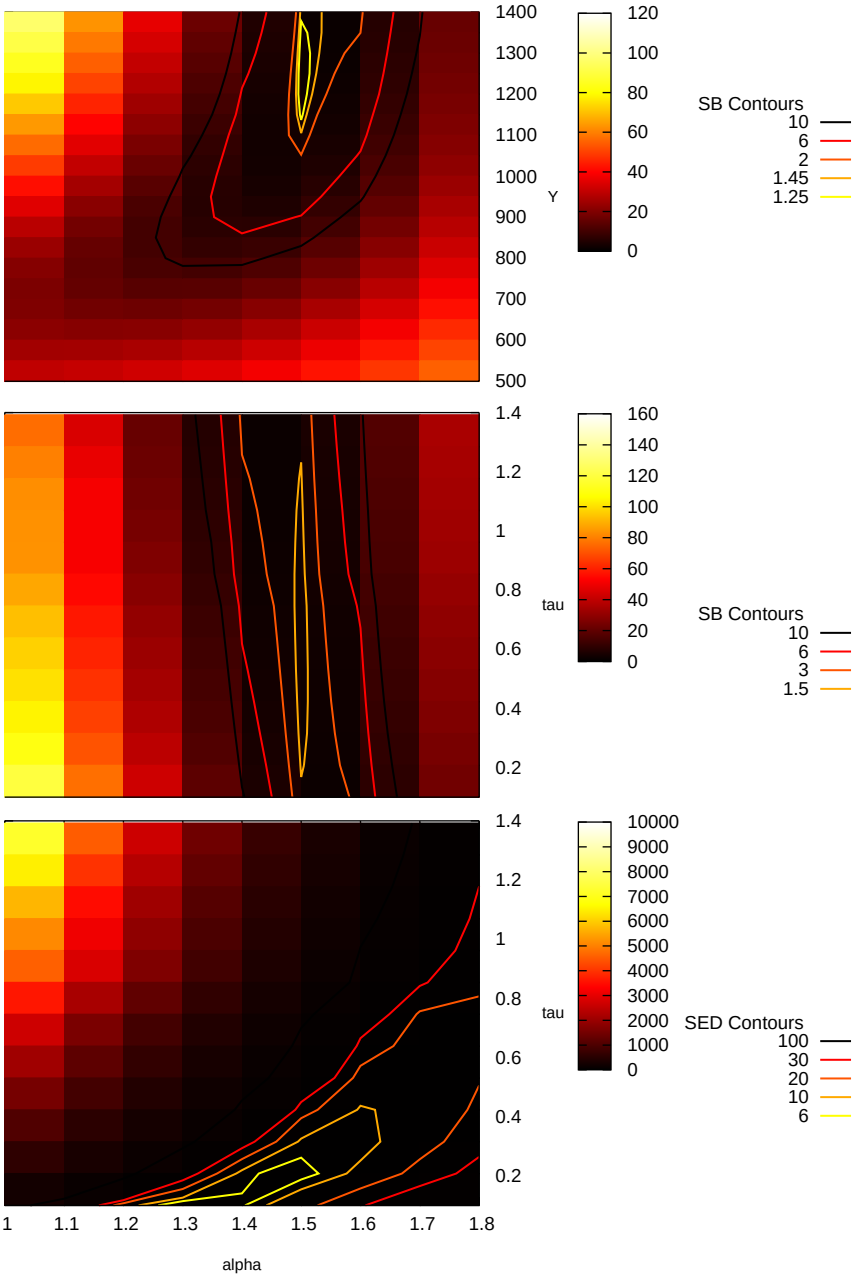

Figure 4.2: Vela IRS 19 Contour plot of χ^2_{SB} (*Top*: $\alpha - Y$ plane, *Middle*: $\alpha - \tau$ plane) and χ^2_{SED} (*Bottom*: $\alpha - \tau$ plane), divided by their respective lowest χ^2_{red}. Contour lines are multiples of the lowest χ^2_{red} of the plane. χ^2_{red} values can be found in Table 4.1

The best fit is determined by calculating the reduced-χ^2 between each model and the observational data. The χ^2_{red} for these fits are not expected to show statistically "good" fits. Rather, these fits are chosen as being better than than other models within the context of this research. It shouldn't be surprising if the χ^2_{red} do not give numerical values indicative of a good fit. There are a number of reasons for this. The SEDs are produced from flux data from different wavelengths and different instruments with different beam sizes and resolutions. Although the beam and source sizes are attempted to be corrected for, it is very unlikely that these are consistent between all observations and are all correct. For example, fluxes are measured with round apertures but these sources are not round. There is also a question of whether or not the different instruments used are all pointing at the exact same position. Other emission features, such as Polycyclic Aromatic Hydrocarbon bending modes and other line contamination varying from one band to another, are not accounted for in DUSTY modelling. Another problem with expecting statistically good fits from χ^2_{red} fitting is in the surface brightness profile fitting. As seen in Figures 2.1 and 2.2, the sources in this work are not spherically symmetric. A more complex model could have been made to account for this non-sphericity but this would introduce more parameters to solve for without necessarily improving χ^2_{red}. An attempt was made to include non-sphericity into the error but it was not necessarily the optimum method.

The reduced-χ^2 is calculated using the following:

$$\chi^2 = \sum_{i=1}^{N} \frac{(Obs_i - Model)^2}{Error_i^2} \tag{4.4}$$

$$\chi^2_{red} = \frac{\chi^2}{\nu} \tag{4.5}$$

$$\nu = N - n - 1 \tag{4.6}$$

Where N, n are the number of data points and number of parameters being fitted for, respectively (Bevington & Robinson, 1992). This calculation takes the difference between model and observation at each data point, turns it into a factor of the error, then divides the sum of the squares by ν. The resultant χ^2_{red} is a measure of goodness of fit of the model, where $\chi^2_{red} \simeq 1$ is an optimal fit because the difference between the model at each data point tends to be a factor of < 1 of the error. Note that for the rest of this paper χ^2_{SB} and χ^2_{SED} are the χ^2_{red} of the surface brightness profiles and SEDs, respectively.

Before the surface brightness profile of the DUSTY model can be evaluated the beam pattern of the telescope used to make the observations must be taken into account. The observations were made using the Swedish-ESO Submillimetre Telescope (SEST) and the beam at a wavelength of 1.2mm, which has been found to fit to a Gaussian with a Half Power Beam Width (HPBW) of $24''$(Nyman *et al.*, 2001). The DUSTY Surface Brightness Profile needs to be convolved with this Gaussian for it to be comparable to the observational data.

The surface brightness output from DUSTY is a 1D profile of intensity vs. distance from the centre of the YSO, in units of Jy arcsecond^{-2}. Using this, a 2D map is made on a 201 by 201 grid. The grid is chosen in such a way that it represents a circularly symmetric source that spans $100''$ in radius from the central pixel, and each pixel represents an arcsecond^2 space, chosen because

of the units of the surface brightness profile outputted by DUSTY. The centre pixel 101×101 is assigned the highest value from the DUSTY output that is between 0-1 arcseconds. Every other point on the grid is assigned based on distance from the centre in arcseconds; the grid point 101x102 would then be 1 arcsecond away. With every grid point (x,y) being $r = \sqrt{\Delta x^2 + \Delta y^2}$ arcseconds from the centre, an intensity that is interpolated from the two nearest DUSTY output values on either side of r is assigned to that grid point. Since this is circularly symmetric only a 1D strip of this grid needs to be convolved with the Gaussian.

The Gaussian function is expressed as $G = Ae^{-\frac{r^2}{2c^2}}$, where $c = \frac{\mathrm{HPBW}}{2\sqrt{2\ln 2}}$, and A is arbitrary, as the whole map is normalized by the central value in the end and so is cancelled out. From the centre to $100''$, each grid point is convolved with the gaussian by

$$Conv(x,y) = \sum_{l=0}^{200}\sum_{m=0}^{200} Flux(l,m) \times \exp\left[-\frac{\sqrt{(l-x)^2-(m-y)^2}}{2c^2}\right] \quad (4.7)$$

It is this new 1D profile that is compared with observational data to see if the particular model fits.

4.3 Modelling Results

	α	Y	τ	$\chi^2_{red}[*,*]_*$
Vela IRS 17	1.35	1325	0.9	$[\alpha, Y]_{SB}$= 3.975
				$[\alpha, \tau]_{SB}$= 3.975
				$[\alpha, \tau]_{SED}$= 15.05
Vela IRS 19	1.5	1050	0.2	$[\alpha, Y]_{SB}$= 1.343
				$[\alpha, \tau]_{SB}$= 1.343
				$[\alpha, \tau]_{SED}$= 6.248

Table 4.1: These are the values of the parameters to be adopted for the DUSTY models that will be used to created density and temperature profiles for RATRAN modelling. They were chosen using a χ^2_{red} fitting approach detailed in the text.

After the surface brightness profile from each model is convolved with the SEST beam's Gaussian profile χ^2_{SB} is calculated for each model within the the full range of α, $t\tau$, and Y. A contour plot of χ^2_{SB} on the α vs. Y plane can be seen at the top of Figure 4.1. At this point, the lowest χ^2_{SB} is used to pick the α and Y to be used to in fitting the SEDs. With this α and Y set, χ^2_{SED} is calculated for the range of $\tau = 0.1 - 1.5$, and the τ from the model with the lowest χ^2_{SED} is chosen. A plot of χ^2_{SED} in the α - τ plane is in Figure 4.1 on the bottom. This process is done again, but the τ found with the first round of fitting is used while fitting within the α and Y range. α and Y are fitted for using the surface brightness profiles; with those values, τ is once again fitted for using SEDs. Other iterations are performed to test for convergence. Uncertainty in these

values is found by changing a parameter by a step, forward and backward, until the difference in χ^2_{red} from the best fit is $> 25\%$; thus is taken as the average between steps forward and backward.

For Vela IRS 17, successive iterations yielded similar sets of α, Y, and τ, and so the average between the two was used. Thus, for Vela IRS 17, $\alpha = 1.35 \pm 0.1, Y = 1325 \pm 100, \tau = 0.9 \pm 0.35$. The same method done for Vela IRS 19 finds that $\alpha = 1.5 \pm 0.1, Y = 1050 \pm 150, \tau = 0.2 \pm 0.1$.

Table 4.1 shows the best fits with their χ^2_{red} in the different planes of the modelled parameter space. Figures 4.1 and 4.2 show the χ^2_{red} values in their respective parameter plane. Figures 4.3 and 4.4 show the surface brightness profiles and SEDs of the best fits along with other outputs from models with parameters outside of the error range. As seen in the right side of Figure 4.4, a model with $\tau = 0.3$ may provide a better fit for the SED, however, this would require Y to be 1250 which would be far too large for the surface brightness profile shown in the left side of the figure.

The temperature profile that DUSTY outputs, along with the input density profile, plotted in Figure 4.5, are what is necessary to move forward with RATRAN modelling.

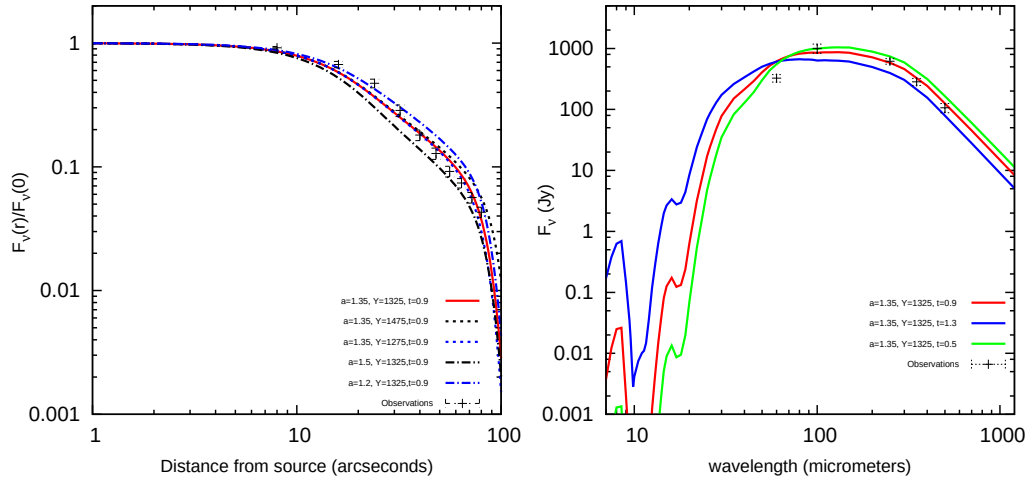

Figure 4.3: Vela IRS 17 - *Left*: Normalized Surface Brightness profiles of DUSTY model. *Right*: SEDs of DUSTY model. The adopted model for Vela IRS 17 has $\alpha = 1.35 \pm 0.1, Y = 1325 \pm 100, \tau = 0.9 \pm 0.35$. χ^2_{red} values can be found in Table 4.1. Also plotted are DUSTY models with values outside the estimated error of the adopted model.

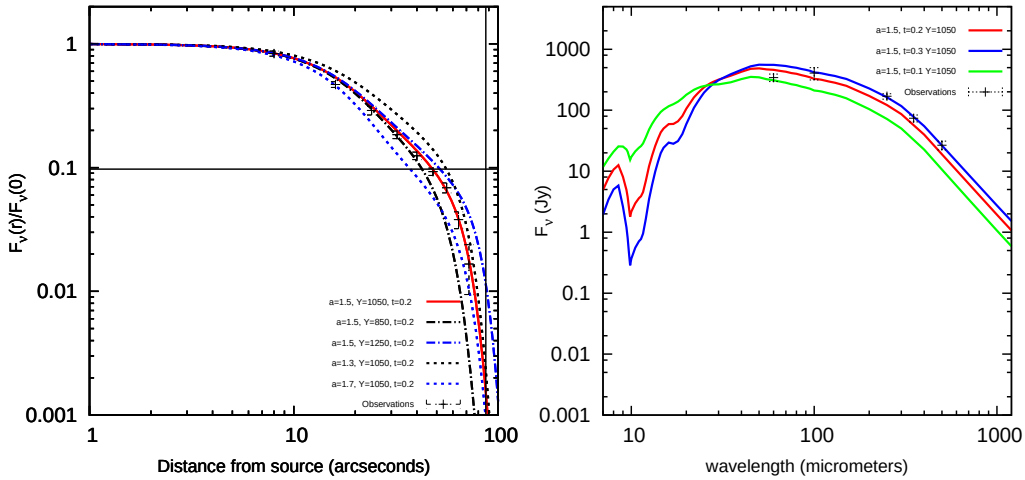

Figure 4.4: Vela IRS 19 - *Left*: Normalized Surface Brightness profiles of DUSTY model. *Right*: SEDs of DUSTY model. The adopted model for Vela IRS 17 has $\alpha = 1.5 \pm 0.1, Y = 1050 \pm 150, \tau = 0.2 \pm 0.1$ χ^2_{red} values can be found in Table 4.1. Also plotted are DUSTY models with values outside the estimated error of the adopted model.

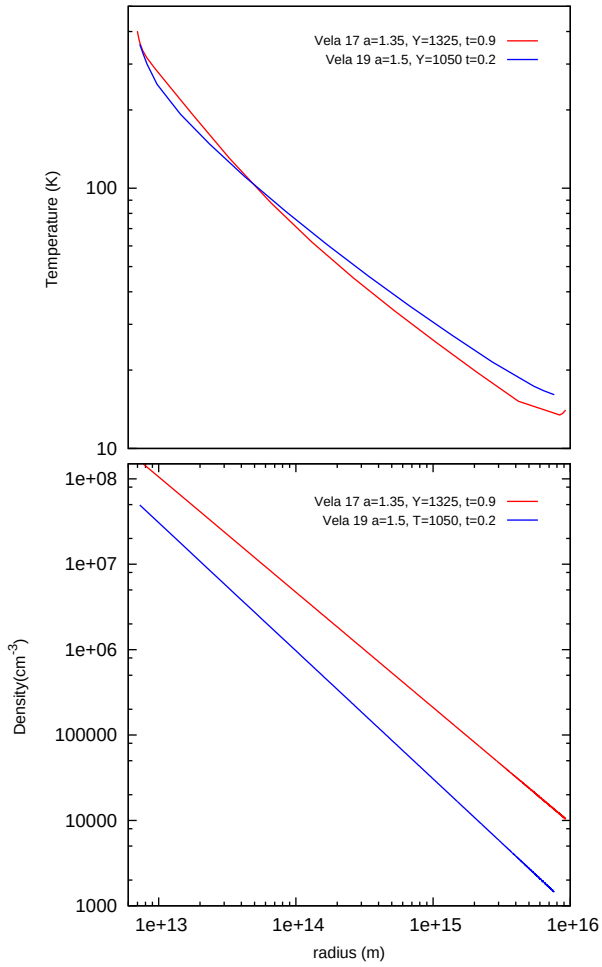

Figure 4.5: Temperature(*Top*) and Density(*Bottom*) profiles of best-fit DUSTY models for Vela IRS 17 (*Red*) and Vela IRS 19 (*Blue*).

Solving for ρ_0 in equation 4.3 we can solve for density of the dust in the envelope in terms of α, τ, and r_i and r_o, the inner and outer radii of the envelope, respectively.

$$\rho(r) = \rho_0 r^{-\alpha} \tag{4.8}$$

$$\rho_{dust}(r) = \frac{\tau_\nu}{\kappa_\nu}(1-\alpha)\left[r_o^{1-\alpha} - r_i^{1-\alpha}\right]^{-1} \tag{4.9}$$

which can then be integrated with the volume to give the mass:

$$M_{dust} = 4\pi \int \rho_{dust}(r) r^2 dr \tag{4.10}$$

$$M_{dust} = \frac{\tau_\nu}{\kappa_\nu}(1-\alpha)\left[r_o^{1-\alpha} - r_i^{1-\alpha}\right]^{-1} \int_{r_i}^{r_o} r^{-\alpha} r^2 dr \tag{4.11}$$

$$M_{dust} = 4\pi \frac{\tau_\nu}{\kappa_\nu} \frac{(1-\alpha)}{(3-\alpha)} \frac{\left[r_o^{3-\alpha} - r_i^{3-\alpha}\right]}{\left[r_o^{1-\alpha} - r_i^{1-\alpha}\right]} \tag{4.12}$$

Assuming $M_{gas} = 100 M_{dust}$, the values in Table 4.1 give a mass of the molecular envelope of 105 $M_\odot$ and 9.0 $M_\odot$ for Vela IRS 17 and Vela IRS 19, respectively. These values are similar to those found by the BLAST survey, which were 98.0 $\pm$ 10.6 $M_\odot$ and 16.5 $\pm$ 2.3 $M_\odot$ for Vela IRS 17 and Vela IRS 19, respectively(Olmi *et al.*, 2009).

DUSTY modelling does have its limitations. As mentioned above, it models with spherical symmetry while the sources themselves do not exhibit circular symmetry in the continuum maps. As well, DUSTY models only a dust continuum as the coolant in the environment while molecular lines, like significant coolants such as molecular lines due to CO and H_2O, are not considered in the transfer of energy in this system. Small dust and Polycyclic Aromatic Hydrocarbons(PAHs) are not taken into account and so their effect on DUSTY's continuum output is missing. Results in Table 4.1 show SED fits are much worse than surface brightness profile fits.

Limitations of DUSTY aside, the modelling and fitting has provided constraints on some physical properties of the environments of the YSOs. With the power law of the density profile, envelope size, and optical depth, DUSTY produces the temperature and density profiles that are required for RATRAN.

Chapter 5

RATRAN Modelling

As mentioned in the introduction, the purpose of this work is to use Herschel-HIFI observations and molecular radiative transfer modelling together to put constraints on the physical and chemical properties of intermediate-mass star forming regions. The program RATRAN, made by Michiel Hogerheijde and Floris van der Tak, is used to model the spectral profiles that are to be compared against the HIFI data (Hogerheijde & van der Tak, 2000). As mentioned in Chapter 3, measurements of water transitions lines were divided into Gaussian profiles to isolate different components of the environment. RATRAN is used to model the radiative transfer and molecular excitation in order to produce spectral profiles that are to be compared with the Gaussian profiles. The environmental conditions of the sources studied will be constrained by the best-fitting input parameters of the adopted models.

5.1 What is RATRAN?

Line emission from molecules in the sub-millimetre and infrared wavelengths are useful tools in the study of embedded star formation. The program RATRAN was developed to calculate the radiative transfer and molecular excitation in dense and cool regions of the interstellar medium to produce line emission spectra. These modelled spectra can then be compared to observed spectra to constrain the physical conditions in the emitting region. For the purposes of this study, it is line emission from water that is to be investigated to interpret the Herschel data.

To model the line emission RATRAN calculates the radiative transfer of energy through the molecular envelope. Radiative transport is the exchange of energy between a radiation field and the medium it passes through by means of absorption, emission, or scattering from atoms or molecules within the medium by photons. The radiation field adds energy into the medium, exciting molecules into higher electrical orbital, vibrational, or for the case of RATRAN and the purpose of this work, rotational levels. After some time the higher states decay into lower states, emitting energy back into the radiation field.

The equation of radiative transport is:

$$\frac{dI_\nu}{ds} = -\alpha_\nu I_\nu + j_\nu \tag{5.1}$$

or when substituting ds with $d\tau_n u \equiv \alpha_\nu ds$

$$\frac{dI_\nu}{d\tau_\nu} = -I_\nu + S_\nu \tag{5.2}$$

where I_ν is the intensity at frequency ν along the line of sight, S_ν is the source function, which is defined as j_ν/α_ν, where j_ν is the emission coefficient with units of erg s $^{-1}$ cm 3 $^{-3}$ Hz $^{-1}$ sr^{-1} and α_ν is the absorption coefficient in units of cm $^{-1}$ (Hogerheijde & van der Tak, 2000; Hillier, 2008).

Both dust and gas are considered sources of emission and absorption in this model, and the emission and absorption coefficients are divided into these two components, leaving them expressed as $\alpha_\nu = (\alpha_\nu(gas) + \alpha_\nu(dust))$ and $j_\nu = (j_\nu(gas) + j_\nu(dust))$. The dust components of the coefficients are given by

$$j_\nu(dust) = \alpha_\nu(dust) B_\nu(T_{dust}) \tag{5.3}$$

$$\alpha_\nu(dust) = \kappa_\nu \rho_{dust} \tag{5.4}$$

where $B_\nu(T_{dust})$ is the Planck function at the dust temperature, ρ_{dust} is the density of the dust, and κ_ν is the dust opacity in cm $^{-2}$ per unit dust mass. As mentioned in Chapter 4, the Ossenkopf & Henning (1994) dust opacities are used for DUSTY modelling. There are opacity options available for RATRAN that come default with the program. This work used the 'jena,thin,e6' option for opacity, which uses the same opacities found by Ossenkopf & Henning (1994). The gas components of the emission and absorption coefficients depend on transitions between upper and lower levels of rotational states. They are

$$j_\nu^{ul}(gas) = \frac{hv_0}{4\pi} n_u A_{ul} \phi(\nu) \tag{5.5}$$

$$\alpha_\nu^{ul}(gas) = \frac{hv_0}{4\pi} (n_l B_{lu} - n_u B_{ul}) \phi(\nu) \tag{5.6}$$

where ϕ accounts for Doppler broadening due to a turbulent velocity field, assumed to be Gaussian:

$$\phi(\nu) = \frac{c}{b\nu_0} \exp\left(-\frac{c^2(\nu-\nu_0)^2}{v_0^2 b^2}\right) \tag{5.7}$$

where c is the speed of light and b is the full width at half maximum in km s^{-1}. A_{ul}, B_{lu}, and B_{ul} are Einstein coefficients which are the probabilities for spontaneous emission and absorption as well as stimulated emission, respectively and are dependant on the molecule.

The population level densities n_u and n_l are determined through the equation of statistical equilibrium:

$$n_l \left[\sum_{k<1} A_{lk} + \sum_{k\neq l} (B_{lk} J_\nu + C_{lk})\right] = \sum_{k>1} n_k A_{kl} + \sum_{k\neq l} n_k (B_{kl} J_\nu + C_{kl}) \tag{5.8}$$

which is calculated for every level. C_{lk} are the collision rates which depend on density, temperature, and collisional rate coefficients of the molecules involved. J_ν is the local mean intensity of the radiation field, given as

$$J_\nu = \frac{1}{4\pi}\int I_\nu d\Omega \tag{5.9}$$

the radiation from all solid angles, Ω, and I_ν is intensity at frequency ν, the same intensity in equation 5.2 that is being modelled. To produce emission spectra of rotational transitions, RATRAN cycles through equation 5.2 through 5.9 using Monte Carlo integration techniques until the population level densities n_u and n_l stabilize. Ray tracing is then used to produce the emission spectra from these population levels (Hogerheijde & van der Tak, 2000).

5.1.1 How it works

Accelerated Monte Carlo (AMC) is the first program used by RATRAN. Starting with the density and temperature profile produced by DUSTY and assuming $T_{gas} = T_{dust}$, the molecular envelope is divided into radial cells and the radiative transfer is reduced to a 1-Dimensional calculation. Testing whether the assumption $T_{gas} = T_{dust}$ is true across the entire star forming region is outside the scope of this work. It was, however, suggested recently at a workshop at the WISH Team annual meeting in Ringberg that in hot regions, close to the YSO, there are indications that $T_{gas} = 100 + T_{dust}$. Scattering can be ignored as it is not important for the wavelengths of interest ($> 10\mu$m) (Hogerheijde & van der Tak, 2000).

Using input parameters detailed in the following Section 5.2, a guess is made at the level populations. Then N number of photons are added to each cell at random positions, pointing randomly in either an inward or outward direction, and given a random frequency ν_r which can be expressed as$|\nu_0 - \nu_r| \leq 4.3b$ where b is the turbulent velocity. The distance from the origin of a ray to the cell boundary, ds, is calculated and the mean radiation field J_ν for each cell is calculated by summing together all the attenuated rays on its boundaries. This J_ν is used to calculate level populations in each cell, which in turn changes the emission and absorption coefficients and how the rays are attenuated along their path to the next cell boundary. The ray changes directions randomly from cell to cell as well.

The cycling between calculating J_ν and level populations continues until the difference between level populations from one iteration to the next is $\leq 10^{-6}$. This whole process is repeated again until the level populations converge to a user-specified accuracy. Once the level populations for the envelope are known the emission profiles can be produced from ray tracing, which is performed by the second program within RATRAN known as SKY. SKY outputs the brightness temperatures at different velocity slices into a FITS (Flexible Image Transfer System) image. The image is 3-dimensional - 2 spatial dimensions and 1 velocity dimension. The brightness temperature is then converted into antenna temperature by convolving the spectra with the beam pattern of the observing telescope, which in this case is the pattern of the Herschel Space Observatory's 3.1 meter telescope (Hillier, 2008).

5.2 Input parameters

As mentioned in Section 5.1.1, several input parameters are needed to run RATRAN. The AMC program starts by modelling the environment in question, which in this case is a spherically symmetric envelope around a young stellar object. Fitting DUSTY models to observational data has provided a temperature and density profile along with inner and outer envelope. In this work it is assumed that the dust and gas have the same temperature, and the ratio between dust and gas mass is 1:100. The number of cells that the envelope is divided into as well as the number of photons randomly deposited within each cell are required; the number of photons is initially set at 1000 for all cases, but RATRAN increases this number on subsequent iterations if necessary. The turbulent velocity is represented by the parameter b in Equation 5.7, and the abundance of water at the inner and outer boundaries relative to H_2 are the remaining input parameters. It is the relative inner and outer abundances and turbulent velocities that are to be constrained by comparing RATRAN models with HIFI observations.

5.3 Limitations of RATRAN

There are limits to modelling line emission when using RATRAN. For one, it assumes spherical symmetry and models only in 1 Dimension. As well, it assumes statistical equilibrium when it is possible that the envelope could be heating up or there be non-equilibrium chemistry at play. There may also be an external radiation field that has an effect, but while DUSTY modelling took that into account, RATRAN does not. Another important effect that is not accounted for in this modelling is the radial motions of the envelope. RATRAN is able to model this but such modelling was beyond the scope of this work.

5.4 Modelling approach

As shown in Chapter 3, emission spectra observed by HIFI can be decomposed into as many as three Gaussian profiles of varying amplitude and FWHM. The narrow, medium, and broad Gaussian components of the overall emission are each associated with different regions of of the star forming region, namely the core, turbulent envelope, and outflowing gas. Only the narrow and medium components of the envelope will be investigated through RATRAN modelling in this work.

Water abundances at the inner and outer edge of the envelope are expressed relative to molecular hydrogen. With a relative inner abundance of 10^{-x} and relative outer abundance of 10^{-y}, models were run within the ranges $x = \{4 : 7\}$ and $y = \{5 : 8\}$. Models were run with x and y incrementing first in steps of 1. The difference between the amplitude of the RATRAN models and the Gaussian profiles was calculated. When two consecutive values of y would show one model with too strong of a profile and the next with too weak of a profile they were chosen as upper and lower bounds. With the lower bound, y_{low}, models were then run with the outer abundance ranging from 1-9$\times 10^{y_{low}}$. For modelling of the narrow components the turbulent velocity was initially set as 1 km s^{-1} and adjusted by increments of 0.1 km s^{-1} as needed. For the medium components

the turbulent velocity was first set at 3 km s^{-1} and then adjusted as needed, first by increments of 1 km s^{-1}, then by 0.1 km s^{-1}.

5.5 Results

The constrained RATRAN input parameters are shown in Table 5.1. Plotted in Figures 5.1, 5.2, 5.4, and 5.5 are the best-fit RATRAN models plotted with the the Gaussians of decomposed spectra from HIFI observations.

Source	Component	Inner abundance	Outer Abundance	b (km s^{-1})
Vela IRS 17	Medium	10^{-4} - 10^{-6}	(6±1) $\times 10^{-8}$	(1.7±1)
Vela IRS 19	Narrow	10^{-4} - 10^{-6}	(6±1) $\times 10^{-8}$	(0.6±1)
	Medium	10^{-4} - 10^{-6}	(4±1) $\times 10^{-7}$	(2.5±1)

Table 5.1: RATRAN input parameters constrained by comparing modelled emission spectra to HIFI measured spectra decomposed into separate Gaussian profiles. For both Vela IRS 17 and Vela IRS 19, the 752 GHz line was the most useful in putting constraints on the outer abundances of H_2O relative to H_2. The inner abundances could not be constrained as well as the outer abundances. No RATRAN model was able to reproduce the narrow component of Vela IRS 17 emission lines and so are not included in this table.

5.5.1 Vela IRS 17

	Medium Component (v=1.7 km s^{-1})		Narrow Component (v=0.7 km s^{-1})	
Line	Flux (K)	$\int T d\nu$ (K km s^{-1})	Flux (K)	$\int T d\nu$(K km s^{-1})
752	0.4148	1.693	-	-
987	absorption	1.383	-	-
557	absorption	-0.126	absorption	0.0884
1113	absorption	-1.439	absorption	-1.439
1153	0.0507	0.157	-	-

Table 5.2: Line profile properties for the RATRAN model of the medium component of Vela IRS 17. The model was set with an inner abundance of $10\times^{-4}$ and outer abundance 6×10^{-8}. There were no constraints put on the abundances using the narrow component; listed here are values of line profiles with the same inner and outer abundances found for the medium component.

Modelled emission spectra for Vela IRS 17 are displayed in Figures 5.1 and 5.2 in the following order: 752 GHz, 987 GHz, 557 GHz, 1113 GHz, and 1153 GHz. A medium component was found for the 752 GHz, 987 GHz, 557 GHz, 1113 GHz, and 1153 GHz lines, while only the 557 GHz and 1113 GHz lines exhibited narrow components. The best fits to the medium and narrow components are plotted with the broad component subtracted HIFI data in Figure 5.3.

As seen in the top left of Figure 5.1, the 752 GHz line shows to be the most useful in putting constraints on the input parameters for RATRAN. The Gaussian line profiles for the medium component can be reproduced through

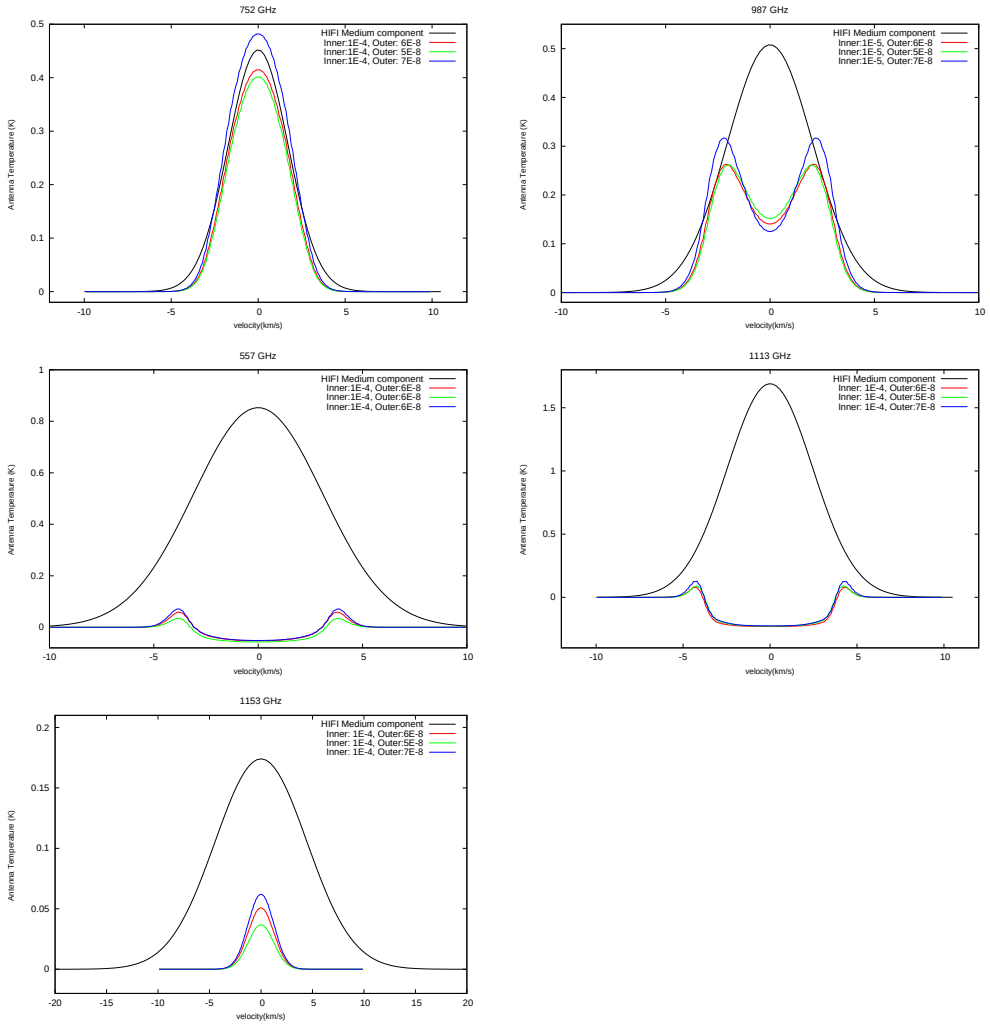

Figure 5.1: RATRAN models of the medium component of Vela IRS 17 H_2O emission lines. These models have an inner abundance of 10^{-4}, while the outer abundance varies from 5-7$\times 10^{-8}$. The turbulent velocity was set to 1.7 km s^{-1}.

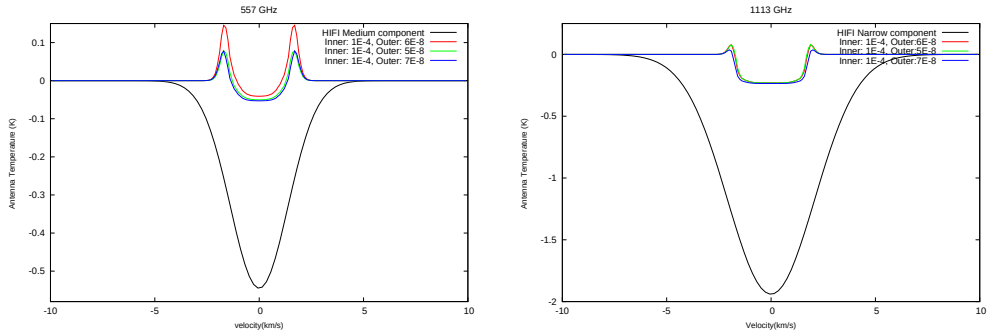

Figure 5.2: RATRAN models of the narrow component of Vela IRS 17 H_2O emission lines. The abundances are the same as in Figure 5.1, but with the turbulent velocity set to 0.7 km s^{-1}.

RATRAN emission line modelling. The plotted line is the model with an inner abundance relative to H_2 of 10^{-4}, outer abundance $(6 \pm 1) \times 10^{-8}$, and a turbulent velocity of (1.7±1) km s^{-1}. However modelling had shown that the inner abundance could not be constrained and could in fact be anywhere between $10^{-4} - 10^{-6}$. Modelled emission for the 987 GHz line can be seen in the top right of Figure 5.1. Outside of the centre of the line it appears to nearly reproduce the Gaussian obtained from HIFI measurements like in the case of the 752 GHz like, but falls short due to absorption in the centre. The modelled emission line for 1153 GHz is too weak to compare at all. For both the 557 GHz line and 1113 GHz line, models show absorption the medium components of the HIFI data show emission. Their wings also fail to follow as closely to the Gaussian profiles as models of the 987 GHz line.

5.5.2 Vela IRS 19

Modelled emission spectra for Vela IRS 19 is shown in Figures 5.4 and 5.5 in the following order: 752 GHz, 987 GHz, 557 GHz, and 1113 GHz. A medium component was found for the 752 GHz, 987 GHz, 557 GHz, and 1113 GHz lines, while narrow components were found for the 752 GHz, 987 GHz, and 1113 GHz lines. The best fits to the medium and narrow components are plotted with the broad component subtracted HIFI data in Figure 5.6.

	Medium Component (v=2.5 km s^{-1})		Narrow Component (v=0.6 km s^{-1})	
Line	Flux (K)	$\int T d\nu$ (K km s^{-1})	Flux (K)	$\int T d\nu$(K km s^{-1})
752	0.1032	0.621	0.0664	0.0978
987	absorption	0.692	absorption	0.1058
557	absorption	0.0227	-	-
1113	absorption	-0.3188	absorption	-0.0791

Table 5.3: Line properties for the RATRAN model. The narrow component was modelled with an inner abundance of $10\times^{-4}$ and outer abundance of 6×10^{-8}. The medium component was modelled with an inner abundance of $10\times^{-4}$ and outer abundance of 4×10^{-7}.

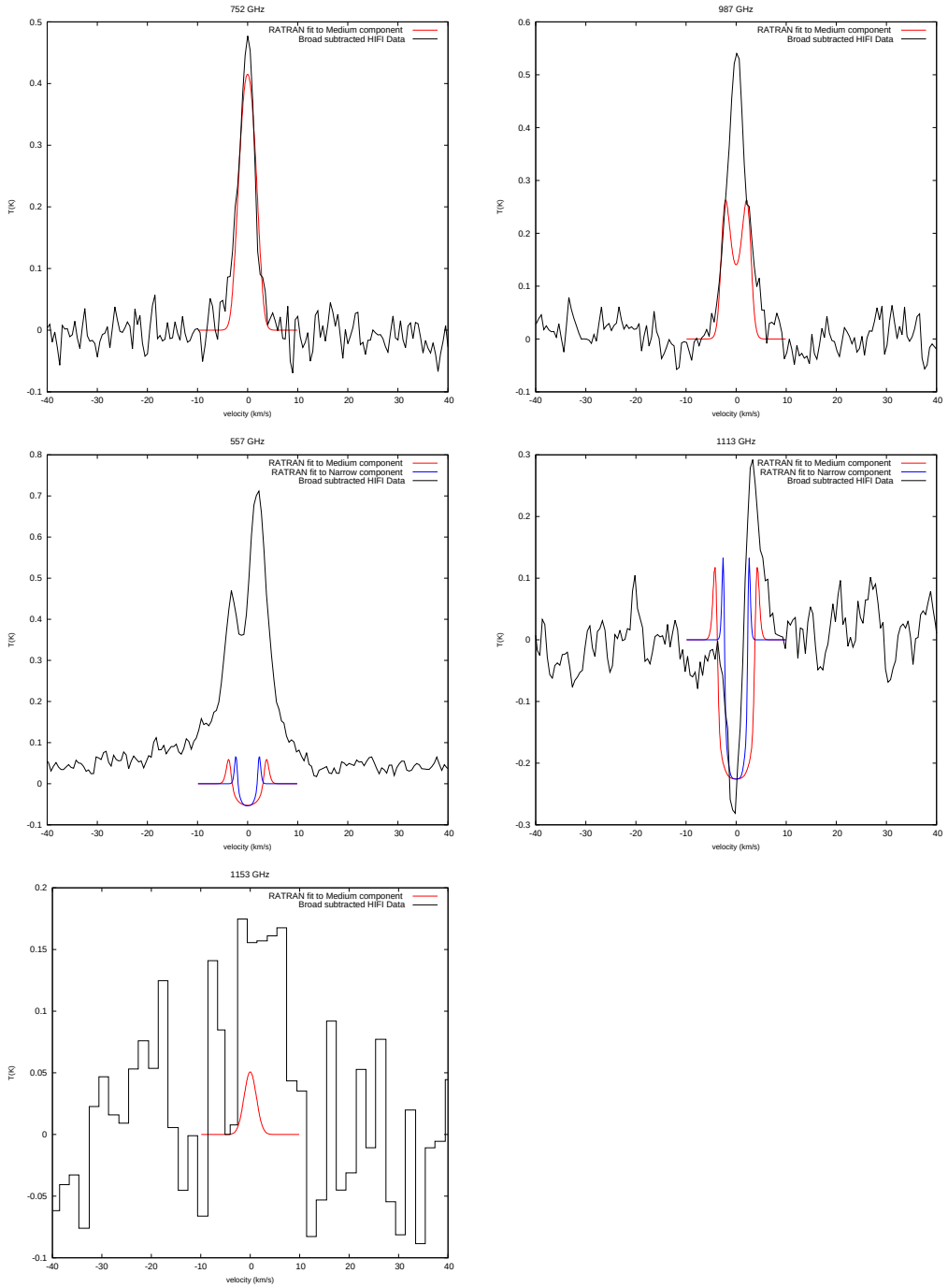

Figure 5.3: Best fit RATRAN models for Vela IRS 17 shown in Table 5.1 and Figures 5.1 and 5.2 plotted against HIFI observations. The HIFI lines in these plots have had their respective broad components subtracted from them. The medium component has an inner abundance of 10^{-6}, an outer abundance of $6{\times}10^{-8}$, and the turbulent velocity is 1.7 km s^{-1}. The narrow component plotted here is not the best fit; what is plotted has an inner abundance of 10^{-6}, an outer abundance of $6{\times}10^{-8}$, and the turbulent velocity is 1.0 km s^{-1}

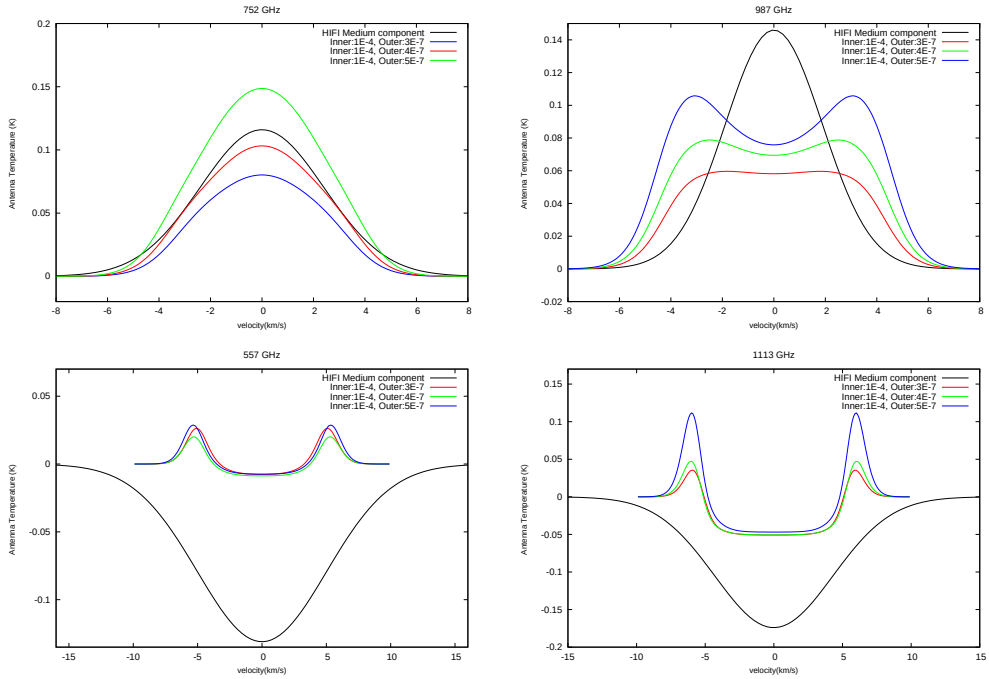

Figure 5.4: RATRAN models of the medium component of Vela IRS 19 H_2O emission lines. These models have an inner abundance of 10^{-4}, while the outer abundance varies from 3-7$\times 10^{-7}$. The turbulent velocity was set to 2.5 km s^{-1}.

Figure 5.4 shows plots of models of the medium component of the HIFI data for Vela IRS 19. The 752 GHz line is again the emission lines that RATRAN modelling came closest to reproducing, with and inner abundance of 10^{-4}–10^{-6}, outer abundance of $(4\pm1)\times10^{-7}$, and a turbulent velocity of (2.5 ± 0.1) km s^{-1}. The 987 GHz line model with these parameters show a more broad emission than the medium component, as well as absorption in the centre of the line. RATRAN models of the 557 GHz and 1113 GHz lines were unable to reproduce the same amount of absorption give in the medium components of these lines.

Figure 5.5 shows models with an inner abundance relative to H_2 of 10^{-4}, outer abundance $(6 \pm 1) \times 10^{-8}$, and a turbulent velocity of (0.6 ± 0.1) km s^{-1}. But as with Vela IRS 17, the inner abundance is not well constrained and can range from $10^{-4} - 10^{-6}$. Modelled emission for the 987 GHz line, seen in the top left of Figure 5.5, fits well to the narrow component of the HIFI data on velocities outside of ν_0, but then shows absorption in the centre of the line. The model of the 1113 GHz line shows absorption and does not fit well to the narrow component of the HIFI data with these parameters.

The results show that, for both Vela IRS 17 and Vela IRS 19, the 752 GHz line is a useful for putting constraints on the abundance of H_2O as well as the turbulent velocity in these star forming regions. With parameters constrained by the 752 GHz line, RATRAN modelling of the 987 GHz line matches well with the Gaussian components at velocities outside of the centre but exhibits absorption at the centre of the line. While both the medium component of Vela

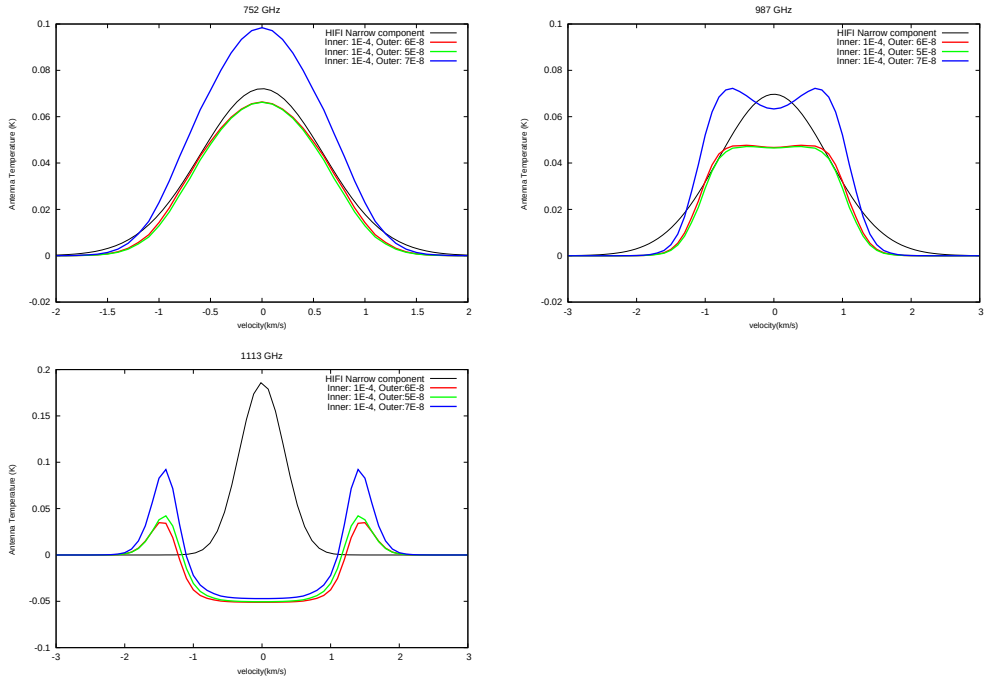

Figure 5.5: RATRAN models of the narrow component of Vela IRS 19 H_2O emission lines. These models have an inner abundance of 10^{-4}, while the outer abundance varies from 5-7$\times 10^{-8}$. The turbulent velocity was set to 0.6 km s^{-1}.

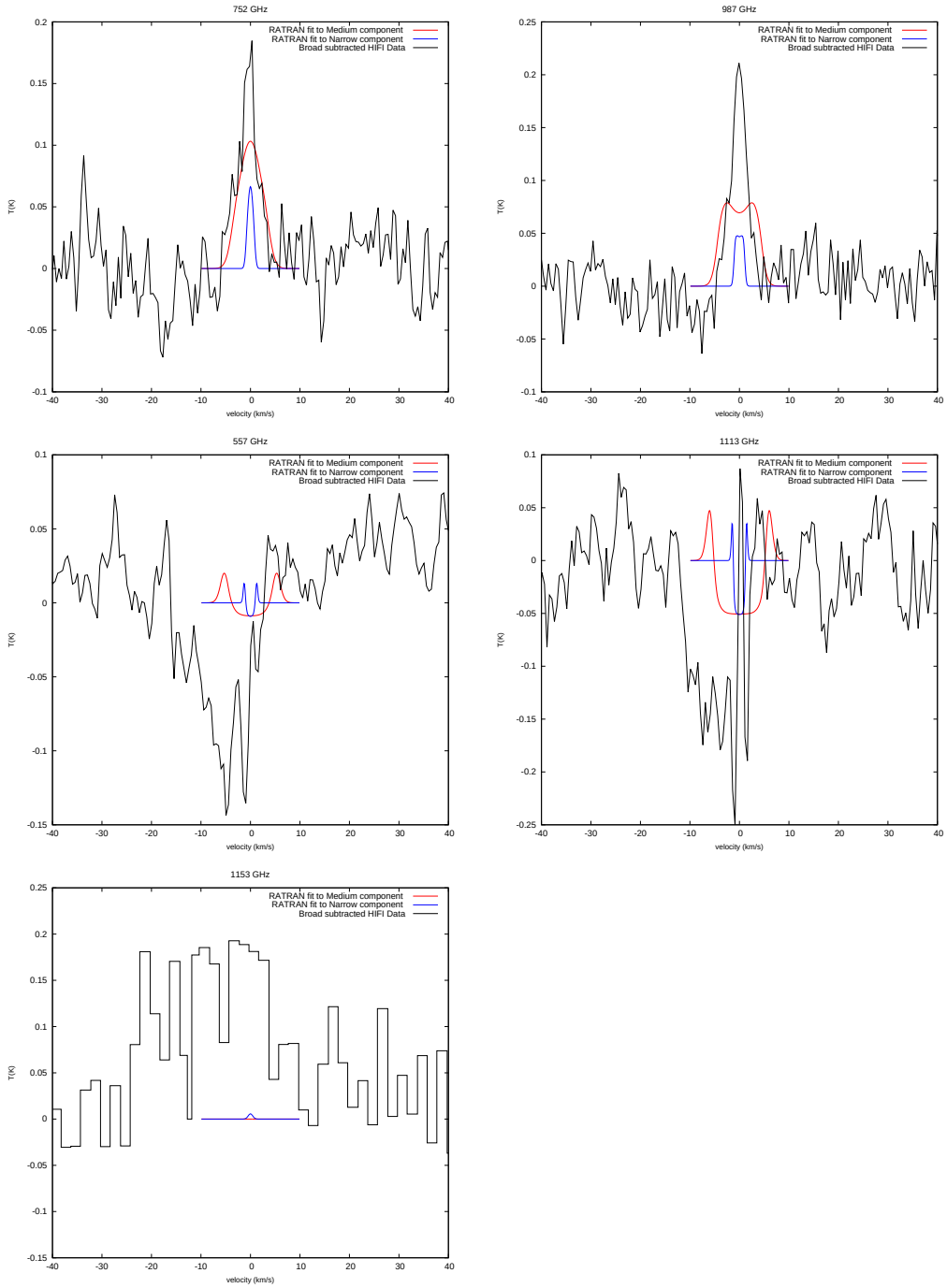

Figure 5.6: Best fit RATRAN models for Vela IRS 19 shown in Table 5.1 and Figures 5.4 and 5.5 plotted against HIFI observations. The HIFI lines in these plots have had their respective broad components subtracted from them. The medium component has an inner abundance of 10^{-6}, an outer abundance of 6×10^{-8}, and the turbulent velocity is 2.5 km s^{-1}. The narrow component plotted here is not the best fit; what is plotted has an inner abundance of 10^{-6}, an outer abundance of 4×10^{-7}, and the turbulent velocity is 0.6 km s^{-1}

IRS 17 and narrow component of Vela IRS 19 are shown through RATRAN modelling to have an outer abundance of $(6 \pm 1) \times 10^{-8}$, the medium component of Vela IRS 19 was reproduced with a model which had an outer abundance of $(4 \pm 1) \times 10^{-7}$, a difference of nearly an order of magnitude.

Chapter 6

Discussion and Conclusions

Star formation is reasonably well understood when it comes to the production of low-mass stars (0.02-2 $M_\odot$), yet an understanding of how high mass stars (>10 $M_\odot$) are formed is not as well developed. There are more IM stars than HM stars in our galaxy and so more opportunities study their formation. Understanding how intermediate-mass (2-10 $M_\odot$) star formation is different from low mass star formation and makes it possible to better understand the conditions necessary for high mass star formation. In this thesis, modelling of molecular emission lines from rotational transitions was performed to put physical and chemical constraints on the environment of two YSO-IM candidates.

The first step in modelling was to use the program DUSTY to model the dust continuum to constrain physical parameters just as the size, density, optical depth, and temperature of the dust in the envelopes surround the YSOs. This was done by fitting to surface brightness profiles and SEDs, and assuming the temperature of the dust at the inner edge of the cloud is 300 K. For Vela IRS 17, using the Steffan-Boltzmann equation to solve for the inner edge, the inner edge of the cloud was calculated to be 6.90×10^{14} cm, and the outer edge of the cloud was found to be $(9.14\pm\ 0.69)\times10^{17}$ cm. A single power law distribution was assumed for the density, and it was found that for $\rho(r) = \rho_0 r^{-\alpha}$, $\alpha = 1.35 \pm 0.1$. For the optical depth at a wavelength of 100μm, $\tau_{100} = 0.9 \pm 0.35$. The same procedure was done for Vela IRS 19. The inner edge of the cloud was calculated to be 7.18×10^{14} cm. Fitting methods then found the outer edge of the cloud to be $(7.54 \pm 0.75)\times10^{17}$ cm, $\alpha = 1.5 \pm 0.1$, and $\tau_{100} = 0.2 \pm 0.1$. Both Vela IRS 17 and Vela IRS 19 have similar a power law index, which suggests their envelopes are similar in their balance between gravity and supporting forces. The DUSTY modelling program produced 1D temperature profiles of the dust in the envelope which, along with the fitted parameters, were used as inputs to for the program RATRAN in the next step of modelling.

Measurements of H_2O molecular emission lines were made using the HIFI instrument aboard the Herschel Space Observatory. The spectra were then decomposed into broad, medium, and narrow Gaussian components. With a model for the structure of the envelope around the YSOs from DUSTY, the program RATRAN was used to model H_2O emission lines to put constraints on the abundance of H_2O relative to H_2, as well as the turbulent velocities.

Although a hypothesis was given of where the different Gaussian components may originate from it is not known for certain. While it is very unlikely that the

broad component originates from within the envelope, the narrow and medium components may, and so are modelled with RATRAN. If the envelope alone produces both the medium and narrow components then a more complicated model, one where turbulent velocity varies with distance, would be required. The idea in this work, however, was to start with the simplest model possible to find if either the medium or narrow components can be reproduced at all.

For Vela IRS 17, RATRAN modelling of the medium component showed an inner abundance in the range of $10^{-4} - 10^{-6}$, the outer abundance more tightly constrained at $(6 \pm 1) \times 10^{-8}$ and a turbulent velocity of 1.7 ± 0.1 km s^{-1}. Modelling of the narrow components was not able constrain these parameters. For Vela IRS 19, RATRAN modelling of the narrow component gave an inner abundance of $10^{-4} - 10^{-6}$, an outer abundance of $(6 \pm 1) \times 10^{-8}$, and a turbulent velocity of 0.6 ± 0.1 km s^{-1}. Modelling of the medium component gave an outer abundance nearly an order of magnitude greater than the narrow component at $(4 \pm 1) \times 10^{-7}$, with a model with a turbulent velocity of 2.5 ± 0.1 km s^{-1}.

Studying the two intermediate-mass candidate YSOs Vela IRS 17 and Vela IRS 19 is useful as they are forming within the same molecular cloud and thus have similar star forming environments. On that same note, the Vela IRS 19 is more deeply embedded than Vela IRS 17, and exhibits weaker molecular lines. However, constraints for the outer abundances found in this work have shown that they may have similar H_2O abundances of $(6 \pm 1) \times 10^{-8}$, with the exception of the medium component of Vela IRS 19, where RATRAN models need the outer abundance to be nearly an order of magnitude greater to be able to model the medium component of the 752 GHz line emission observed by HIFI.

As stated in the introduction, having constraints on the outer abundance gives an idea of the abundance of water relative to H_2 before the YSO began to evolve, while constraints on the inner abundance gives a measure of the total water within the environment. In this work we find the outer abundances to be $\sim 10^{-8}$, with a maximum possible inner abundance of 10^{-6}, which means <1% of water remains in the gas phase in the cold outer regions of the envelope.

The turbulent velocity gives some idea of supporting forces working against gravity. These supporting forces are made up of both thermal and turbulent velocity. Adopting a temperature for the region of 30 K, thermal velocities come out to be ~ 0.2 km s^{-1}. This is much lower than the constraints put on turbulent velocity in this work and thus turbulence completely dominates the support within both Vela IRS 17 and Vela IRS 19. The origins of this turbulence is unclear although may be from interactions with outflows. This support slows the accretion of mass onto the central source.

For both Vela IRS 17 and 19 the 752 GHz line was the most useful in providing constraints on the inner and outer abundances of H_2O. The other modelled lines exhibited too much absorption to be able to fit to the Gaussian components of the decomposed HIFI data, with the exception of the narrow component of Vela IRS 17 and medium component of Vela IRS 19 for the 557 GHz and 1113 GHz lines where models could not produce enough absorption. The inner abundance of H_2O was not able to be constrained as well as the outer abundance which suggests the lines in this study are not sensitive to the inner abundance. This may be an indication that hot inner region gas has a greater affect on higher excitation lines, as the lines in this work have lower excitation temperatures.

While only the 752 GHz line was the most useful in putting constraints on the abundances and turbulent velocities, the lack of fit to the other lines does not necessarily mean there should be a lack of confidence in these constraints. Emission lines with lower excitation lines are more easily affected by material along the line of sight, while lines with higher excitation lines are very weak in comparison to the 752 GHz as they require higher temperatures for their excitation and the volume of hot gas is very small in this model. The 752 GHz line was expected to be a good probe as it is less dependant on the inner hot regions for emission while the surrounding material wouldn't be hot enough to absord or emit in this line. Other lines, like the 987 GHz line, are useful in providing guidance in the fitting; even with foreground and background emission it is hard to mask turbulent velocity widths.

Sources of error in the observational data include noise in the continuum maps used to produce surface brightness profiles, as well as flux error in SED measurements. Both DUSTY and RATRAN are 1D simulations that assume spherical symmetry. RATRAN also assumes statistical equilibrium throughout the envelope and does not account for any external radiation.

One of the main reasons for studying intermediate-mass star formation is to understand how the paradigm for star formation of low mass stars differs from the formation of high mass stars. It is thus important to note the analysis of water emission lines from low and high mass star forming regions. Radiative transfer modelling performed by low and high mass WISH teams have put constraints on water abundances in star forming regions of low and high mass YSO candidates.

For the low mass regime: $H_2^{16}O$ and $H_2^{18}O$ line profiles observed in three deeply embedded protostars in the low-mass star forming region NGC 1333 showed abundances of $H_2O \sim 10^{-5}$-10^{-4} in regions associated with shocks and $\sim 10^{-8}$ in the outer envelope (Kristensen *et al.*, 2010). A survey of H_2O emission from 20 bi-polar outflows of low mass young stellar objects found typical H_2O abundances of 3×10^{-7} corresponding to the warm ($\sim$ 500 K) component of outflowing gas(Tafalla *et al.*, 2013). A study into the outflow of low mass protostar L1448 found similar results for for the abundance in warm regions of outflow of 5-10$\times 10^{-7}$(Nisini *et al.*, 2013; Santangelo *et al.*, 2012).

For the high mass regime: A study into four massive star forming regions by Marseille *et al.* (2010) found, after separating contributions for by outflow and foreground clouds, H_2O abundances in the outer envelopes ranging from 5×10^{-10} to 4×10^{-8}. The region W3 IRS5, which is suspected to host high mass stars in the early stages of evolution, was found to have a similar range of 10^{-8}-10^{-10} for water abundances in the outer envelope (Chavarría *et al.*, 2010). The high-mass protostellar object DR21 was found abundances of $\sim 2 \times 10^{-10}$ in the dense core, $\sim 4 \times 10^{-9}$ in the foreground cloud, and $\sim 7 \times 10^{-7}$ in the outflow (van der Tak *et al.*, 2010).

While the studies of the low mass star forming regions show abundances of water in the outer envelopes of $\approx 10^{-8}$, studies of regions of high mass star formation are finding outer envelope abundances in the range of 10^{-8}-10^{-10}. The work in this theses has found outer envelope abundances of 4×10^{-7}-6×10^{-8}. A study performed on the intermediate-mass protostar NGC 7129 FIRS 2 which found a similar value for the outer abundances of $\approx 10^{-7}$ (Johnstone *et al.*, 2010). This study, along with work done by other members of the WISH-IM team, has begun to put constraints on the outer abundances of water relative

to H_2 in intermediate-mass YSOs for the first time. The emerging picture is showing that the clouds that form IM stars do not start out as cold and dense are high-mass star forming regions and that these IM stars are forming in similar environments as low-mass stars. For the sources studied in this work we've found that the clouds are strongly supported by non-thermal motions.

6.1 Future Work

There are a number of ways to proceed following this work. As mentioned, the lines studied in this work do not seem to be sensitive to the inner abundance of H_2O. These lines have low excitation temperatures and so an examination in H_2O lines with higher excitation temperatures may turn out to be more sensitive and thus prove useful in putting constraints on the inner abundance. Another area of interest would be to incorporate infall velocity in the RATRAN modelling, which was not been taken into account in this work. The 1113 GHz line for Vela IRS 17 exhibits a possible P-Cygni profile; having infall in models of emission lines may improve constraints on the abundance of H_2O for this source. Non-spherical models with LIME may also be useful, as the models in this work assume spherical symmetry which is not a characteristic of the sources in this study.

As it has been stated that other emission lines like the 987 GHz line provide guidance to fitting with the 752 GHz line, the turbulent velocity width that fits with to the 752 GHz for Vela IRS 19 in Figure 5.4 does not fit as well for the 987 GHz line. On that same note, it was found that when re-running RATRAN models with the parameters of the best fit did not yield the exact same result. This shows that Monte Carlo random noise error has a significant effect on the modelled emission. It may very well be that, after reducing random noise by either increasing the number of photons in the model or the number of cells in the geometry, different values for the outer abundance and turbulent velocity could give a better fit that also reconciles the turbulent width of the 752 GHz line with the 987 GHz line.

Finally, mass estimates in Chapter 4 are dependent on α, κ_ν, and τ_ν, where α is well constrained by surface brightness profiles and values of κ_ν by Ossenkopf & Henning (1994) used for this work are well accepted. τ_ν, on the other hand, is constrained using flux measurements made using instruments with large FWHMs. The degree of accuracy of the PACS instrument aboard the Herschel Space Observatory is an improvement compared to flux measurements made with BLAST. DUSTY modelling and fitting to SEDs made from PACS data may result in different values for τ_ν, which would in turn change estimates of the mass of the envelopes around Vela IRS 17 and Vela IRS 19.

Bibliography

Beichman, C.A., Neugebauer, G., Habing, H.J., Clegg, P.E., & Chester, Thomas J. 1988. Infrared astronomical satellite (IRAS) catalogs and atlases. Volume 2: The point source catalog declination range 90 deg greater than delta greater than 30 deg. **2**.

Bevington, Philip R., & Robinson, D. Keith. 1992. *Data reduction and error analysis for the physical sciences, Second addition.* McGraw-Hill.

Black, J. H. 1994. The first Symposium on the Infrared Cirrus and DIffuse Interstellar Clouds. *ASP*, 58, 355.

Carroll, Bradley., & Ostlie, Dale. 2007. *An Introduction to Modern Astrophysics.* Pearson Assidon-Wesley.

Chavarría, L., Herpin, F., Jacq, T., Braine, J., Bontemps, S., Baudry, A., Marseille, M., van der Tak, F., Pietropaoli, B., Wyrowski, F., Shipman, R., Frieswijk, W., van Dishoeck, E. F., Cernicharo, J., Bachiller, R., Benedettini, M., Benz, A. O., Bergin, E., Bjerkeli, P., Blake, G. A., Bruderer, S., Caselli, P., Codella, C., Daniel, F., di Giorgio, A. M., Dominik, C., Doty, S. D., Encrenaz, P., Fich, M., Fuente, A., Giannini, T., Goicoechea, J. R., de Graauw, T., Hartogh, P., Helmich, F., Herczeg, G. J., Hogerheijde, M. R., Johnstone, D., Jørgensen, J. K., Kristensen, L. E., Larsson, B., Lis, D., Liseau, R., McCoey, C., Melnick, G., Nisini, B., Olberg, M., Parise, B., Pearson, J. C., Plume, R., Risacher, C., Santiago-García, J., Saraceno, P., Stutzki, J., Szczerba, R., Tafalla, M., Tielens, A., van Kempen, T. A., Visser, R., Wampfler, S. F., Willem, J., & Yıldız, U. A. 2010. Water in massive star-forming regions: HIFI observations of W3 IRS5. *AAP*, **521**(Oct.), L37.

Crimier, N., Ceccarelli, C., Alonso-Albi, T., Fuente, A., Caselli, P., Johnstone, D., Kahane, C., Lefloch, B., Maret, S., Plume, R., Rizzo, J. R., Tafalla, M., van Dishoeck, E., & Wyrowski, F. 2010. Physical structure of the envelopes of intermediate-mass protostars. *Astronomy and Astrophysics*, **516**(June), A102.

de Graauw, T., Helmich, F. P., Phillips, T. G., Stutzki, J., Caux, E., Whyborn, N. D., Dieleman, P., Roelfsema, P. R., Aarts, H., Assendorp, R., Bachiller, R., Baechtold, W., Barcia, A., Beintema, D. A., Belitsky, V., Benz, A. O., Bieber, R., Boogert, A., Borys, C., Bumble, B., Caïs, P., Caris, M., Cerulli-Irelli, P., Chattopadhyay, G., Cherednichenko, S., Ciechanowicz, M., Coeur-Joly, O., Comito, C., Cros, A., de Jonge, A., de Lange, G., Delforges, B., Delorme, Y., den Boggende, T., Desbat, J.-M., Diez-González, C., di Giorgio, A. M.,

Dubbeldam, L., Edwards, K., Eggens, M., Erickson, N., Evers, J., Fich, M., Finn, T., Franke, B., Gaier, T., Gal, C., Gao, J. R., Gallego, J.-D., Gauffre, S., Gill, J. J., Glenz, S., Golstein, H., Goulooze, H., Gunsing, T., Güsten, R., Hartogh, P., Hatch, W. A., Higgins, R., Honingh, E. C., Huisman, R., Jackson, B. D., Jacobs, H., Jacobs, K., Jarchow, C., Javadi, H., Jellema, W., Justen, M., Karpov, A., Kasemann, C., Kawamura, J., Keizer, G., Kester, D., Klapwijk, T. M., Klein, T., Kollberg, E., Kooi, J., Kooiman, P.-P., Kopf, B., Krause, M., Krieg, J.-M., Kramer, C., Kruizenga, B., Kuhn, T., Laauwen, W., Lai, R., Larsson, B., Leduc, H. G., Leinz, C., Lin, R. H., Liseau, R., Liu, G. S., Loose, A., López-Fernandez, I., Lord, S., Luinge, W., Marston, A., Martín-Pintado, J., Maestrini, A., Maiwald, F. W., McCoey, C., Mehdi, I., Megej, A., Melchior, M., Meinsma, L., Merkel, H., Michalska, M., Monstein, C., Moratschke, D., Morris, P., Muller, H., Murphy, J. A., Naber, A., Natale, E., Nowosielski, W., Nuzzolo, F., Olberg, M., Olbrich, M., Orfei, R., Orleanski, P., Ossenkopf, V., Peacock, T., Pearson, J. C., Peron, I., Phillip-May, S., Piazzo, L., Planesas, P., Rataj, M., Ravera, L., Risacher, C., Salez, M., Samoska, L. A., Saraceno, P., Schieder, R., Schlecht, E., Schlöder, F., Schmülling, F., Schultz, M., Schuster, K., Siebertz, O., Smit, H., Szczerba, R., Shipman, R., Steinmetz, E., Stern, J. A., Stokroos, M., Teipen, R., Teyssier, D., Tils, T., Trappe, N., van Baaren, C., van Leeuwen, B.-J., van de Stadt, H., Visser, H., Wildeman, K. J., Wafelbakker, C. K., Ward, J. S., Wesselius, P., Wild, W., Wulff, S., Wunsch, H.-J., Tielens, X., Zaal, P., Zirath, H., Zmuidzinas, J., & Zwart, F. 2010. The Herschel-Heterodyne Instrument for the Far-Infrared (HIFI). *Astronomy and Astrophysics*, **518**(July), L6.

Elia, D., Massi, F., Strafella, F., De Luca, M., Giannini, T., Lorenzetti, D., Nisini, B., Campeggio, L., & Maiolo, B. M. T. 2007. Mapping Molecular Emission in Vela Molecular Ridge Cloud D. *Astrophysical Journal*, **655**(Jan.), 316–331.

Fuente, A., Caselli, P., McCoey, C., Cernicharo, J., Johnstone, D., Fich, M., van Kempen, T., van Dishoeck, E., Yıldız, U., Visser, R., Kristensen, L., Alonso-Albi, T., Herpin, F., & Tisi, S. 2012. The abundance of $C^{18}O$ and HDO in the envelope and hot core of the intermediate mass protostar NGC 7129 FIRS 2. *Astronomy and Astrophysics*, **540**(Apr.), A75.

Giannini, T., Massi, F., Podio, L., Lorenzetti, D., Nisini, B., Caratti o Garatti, A., Liseau, R., Lo Curto, G., & Vitali, F. 2005. Star formation in the Vela Molecular Clouds: A new protostar powering a bipolar jet. *Astronomy and Astrophysics*, **433**(Apr.), 941–954.

Hartmann, Lee. 1998. *Accretion Processes in Star Formation*. Cambridge University Press.

Herbst, W., & Sawyer, D. L. 1981. Results of a new approach to determining the density function in the galactic plane - The local system. *Astrophysical Journal*, **243**(Feb.), 935–944.

Hillier, Michael. 2008. *Modeling Water Emission from Intermediate Mass Star Formation Regions*. M.Sc. thesis, University of Waterloo, Waterloo, ON., Canada.

Hogerheijde, M. R., & van der Tak, F. F. S. 2000. An accelerated Monte Carlo method to solve two-dimensional radiative transfer and molecular excitation. With applications to axisymmetric models of star formation. *Astronomy and Astrophysics*, **362**(Oct.), 697–710.

in the ESA, Someone. 2011. HIFI Observers Manual. *http://herschel.esac.esa.int/Docs/HIFI/html/hifi.html*.

Ivezic, Z., Nenkova, M., & Elitzur, M. 1999. User Manual for DUSTY. *University of Kentucky Internal Report*, Oct.

Johnstone, D., Fich, M., McCoey, C., van Kempen, T. A., Fuente, A., Kristensen, L. E., Cernicharo, J., Caselli, P., Visser, R., Plume, R., Herczeg, G. J., van Dishoeck, E. F., Wampfler, S., Bachiller, R., Baudry, A., Benedettini, M., Bergin, E., Benz, A. O., Bjerkeli, P., Blake, G., Bontemps, S., Braine, J., Bruderer, S., Codella, C., Daniel, F., di Giorgio, A. M., Dominik, C., Doty, S. D., Encrenaz, P., Giannini, T., Goicoechea, J. R., de Graauw, T., Helmich, F., Herpin, F., Hogerheijde, M. R., Jacq, T., Jørgensen, J. K., Larsson, B., Lis, D., Liseau, R., Marseille, M., Melnick, G., Neufeld, D., Nisini, B., Olberg, M., Parise, B., Pearson, J., Risacher, C., Santiago-García, J., Saraceno, P., Shipman, R., Tafalla, M., van der Tak, F., Wyrowski, F., Yıldız, U. A., Caux, E., Honingh, N., Jellema, W., Schieder, R., Teyssier, D., & Whyborn, N. 2010. Herschel/HIFI spectroscopy of the intermediate mass protostar NGC 7129 FIRS 2. *Astronomy and Astrophysics*, **521**(Oct.), L41.

Jørgensen, J. K. 2004 (Oct.). *Tracing the physical and chemical evolution of low-mass protostars*. Ph.D. thesis, Leiden Observatory, Leiden University, P.O. Box 9513, 2300 RA Leiden, The Netherlands.

Kristensen, L. E., Visser, R., van Dishoeck, E. F., Yıldız, U. A., Doty, S. D., Herczeg, G. J., Liu, F.-C., Parise, B., Jørgensen, J. K., van Kempen, T. A., Brinch, C., Wampfler, S. F., Bruderer, S., Benz, A. O., Hogerheijde, M. R., Deul, E., Bachiller, R., Baudry, A., Benedettini, M., Bergin, E. A., Bjerkeli, P., Blake, G. A., Bontemps, S., Braine, J., Caselli, P., Cernicharo, J., Codella, C., Daniel, F., de Graauw, T., di Giorgio, A. M., Dominik, C., Encrenaz, P., Fich, M., Fuente, A., Giannini, T., Goicoechea, J. R., Helmich, F., Herpin, F., Jacq, T., Johnstone, D., Kaufman, M. J., Larsson, B., Lis, D., Liseau, R., Marseille, M., McCoey, C., Melnick, G., Neufeld, D., Nisini, B., Olberg, M., Pearson, J. C., Plume, R., Risacher, C., Santiago-García, J., Saraceno, P., Shipman, R., Tafalla, M., Tielens, A. G. G. M., van der Tak, F., Wyrowski, F., Beintema, D., de Jonge, A., Dieleman, P., Ossenkopf, V., Roelfsema, P., Stutzki, J., & Whyborn, N. 2010. Water in low-mass star-forming regions with Herschel . HIFI spectroscopy of NGC 1333. *AAP*, **521**(Oct.), L30.

Kwok, Sun. 2007. *Physics and Chemistry of the Interstellar Medium*. University Science Books.

Lada, C. J., & Fich, M. 1996. The Structure and Energetics of a Highly Collimated Bipolar Outflow: NGC 2264G. *ApJ*, **459**(Mar.), 638.

Liseau, R., Lorenzetti, D., Nisini, B., Spinoglio, L., & Moneti, A. 1992. Star formation in the VELA molecular clouds. I - The IRAS-bright Class I sources. *Astronomy and Astrophysics*, **265**(Nov.), 577–596.

Lorenzetti, D., Spinoglio, L., & Liseau, R. 1993. Star Formation in the VELA Molecular Clouds - Part Two - the Luminosity Function of the Class-I Sources. *Astronomy and Astrophysics*, **275**(Aug.), 489.

Marseille, M. G., van der Tak, F. F. S., Herpin, F., Wyrowski, F., Chavarría, L., Pietropaoli, B., Baudry, A., Bontemps, S., Cernicharo, J., Jacq, T., Frieswijk, W., Shipman, R., van Dishoeck, E. F., Bachiller, R., Benedettini, M., Benz, A. O., Bergin, E., Bjerkeli, P., Blake, G. A., Braine, J., Bruderer, S., Caselli, P., Caux, E., Codella, C., Daniel, F., Dieleman, P., di Giorgio, A. M., Dominik, C., Doty, S. D., Encrenaz, P., Fich, M., Fuente, A., Gaier, T., Giannini, T., Goicoechea, J. R., de Graauw, T., Helmich, F., Herczeg, G. J., Hogerheijde, M. R., Jackson, B., Javadi, H., Jellema, W., Johnstone, D., Jørgensen, J. K., Kester, D., Kristensen, L. E., Larsson, B., Laauwen, W., Lis, D., Liseau, R., Luinge, W., McCoey, C., Megej, A., Melnick, G., Neufeld, D., Nisini, B., Olberg, M., Parise, B., Pearson, J. C., Plume, R., Risacher, C., Roelfsema, P., Santiago-García, J., Saraceno, P., Siegel, P., Stutzki, J., Tafalla, M., van Kempen, T. A., Visser, R., Wampfler, S. F., & Yıldız, U. A. 2010. Water abundances in high-mass protostellar envelopes: Herschel observations with HIFI. *AAP*, **521**(Oct.), L32.

Massi, F., Giannini, T., Lorenzetti, D., Liseau, R., Moneti, A., & Andreani, P. 1999. Star formation in the VELA Molecular Clouds. III. Near IR images and MM photometry of D-cloud IRAS sources. *Astronomy and Astrophysics*, **136**(May), 471–490.

Massi, F., de Luca, M., Elia, D., Giannini, T., Lorenzetti, D., & Nisini, B. 2007. Star formation in the Vela molecular ridge. Large scale mapping of cloud D in the mm continuum. *Astronomy and Astrophysics*, **466**(May), 1013–1023.

Mathis, J. S., Rumpl, W., & Nordsieck, K. H. 1977. The size distribution of interstellar grains. *ApJ*, **217**(Oct.), 425–433.

McCoey, Carolyn, Tisi, S., van Kempen, T.A., Fich, M., Johnstone, D., Fuente, A., Caselli, P., van Dischoeck, E., Kristensen, L., & Cernicharo, J. 2013. Water Emission from Intermediate Mass YSO. *In prep.*

Nisini, B., Santangelo, G., Antoniucci, S., Benedettini, M., Codella, C., Giannini, T., Lorenzani, A., Liseau, R., Tafalla, M., Bjerkeli, P., Cabrit, S., Caselli, P., Kristensen, L., Neufeld, D., Melnick, G., & van Dishoeck, E. F. 2013. Mapping water in protostellar outflows with Herschel. PACS and HIFI observations of L1448-C. *AAP*, **549**(Jan.), A16.

Nyman, L.-Å., Lerner, M., Nielbock, M., Anciaux, M., Brooks, K., Chini, R., Albrecht, M., Lemke, R., Kreysa, E., Zylka, R., Johansson, L. E. B., Bronfman, L., Kontinen, S., Linz, H., & Stecklum, B. 2001. SIMBA explores the southern sky. *The Messenger*, **106**(Dec.), 40–44.

Olberg, Michael. 2010. *Beam Observation Towards Mars.*

Olmi, L., Ade, P. A. R., Anglés-Alcázar, D., Bock, J. J., Chapin, E. L., De Luca, M., Devlin, M. J., Dicker, S., Elia, D., Fazio, G. G., Giannini, T., Griffin, M., Gundersen, J. O., Halpern, M., Hargrave, P. C., Hughes, D. H., Klein, J., Lorenzetti, D., Marengo, M., Marsden, G., Martin, P. G., Massi, F.,

Mauskopf, P., Netterfield, C. B., Patanchon, G., Rex, M., Salama, A., Scott, D., Semisch, C., Smith, H. A., Strafella, F., Thomas, N., Truch, M. D. P., Tucker, C., Tucker, G. S., Viero, M. P., & Wiebe, D. V. 2009. The Blast Survey of the Vela Molecular Cloud: Physical Properties of the Dense Cores in Vela-D. *Astrophysical Journal*, **707**(Dec.), 1836–1851.

Ossenkopf, V., & Henning, T. 1994. Dust opacities for protostellar cores. *Astronomy and Astrophysics*, **291**(Nov.), 943–959.

Pilbratt, G. L., Riedinger, J. R., Passvogel, T., Crone, G., Doyle, D., Gageur, U., Heras, A. M., Jewell, C., Metcalfe, L., Ott, S., & Schmidt, M. 2010. Herschel Space Observatory. An ESA facility for far-infrared and submillimetre astronomy. *Astronomy and Astrophysics*, **518**(July), L1.

Pinsonneault, M. H., & Delahaye, F. 2009. The Solar Heavy Element Abundances. II. Constraints from Stellar Atmospheres. *ApJ*, **704**(Oct.), 1174–1188.

Santangelo, G., Nisini, B., Giannini, T., Antoniucci, S., Vasta, M., Codella, C., Lorenzani, A., Tafalla, M., Liseau, R., van Dishoeck, E. F., & Kristensen, L. E. 2012. The Herschel HIFI water line survey in the low-mass proto-stellar outflow L1448. *AAP*, **538**(Feb.), A45.

Stahler, Steven W., & Palla, Francesco. 2004. *The Formation of Stars*. Wiley-VCH.

Tafalla, M., Liseau, R., Nisini, B., Bachiller, R., Santiago-García, J., van Dishoeck, E. F., Kristensen, L. E., Herczeg, G. J., & Yıldız, U. A. 2013. High-pressure, low-abundance water in bipolar outflows. Results from a Herschel-WISH survey. *AAP*, **551**(Mar.), A116.

Tielens, Alexander G G. 2005. *The Physics and Chemistry of the Interstellar Medium*. University University Press, Cambridge.

van der Tak, F., Walmsley, M., Herpin, F., & Ceccarelli, C. 2005. A dust and water disk in AFGL 2591. *Page 312P of: IAU Symposium*. IAU Symposium, vol. 235.

van der Tak, F. F. S., Marseille, M. G., Herpin, F., Wyrowski, F., Baudry, A., Bontemps, S., Braine, J., Doty, S., Frieswijk, W., Melnick, G., Shipman, R., van Dishoeck, E. F., Benz, A. O., Caselli, P., Hogerheijde, M., Johnstone, D., Liseau, R., Bachiller, R., Benedettini, M., Bergin, E., Bjerkeli, P., Blake, G., Bruderer, S., Cernicharo, J., Codella, C., Daniel, F., di Giorgio, A. M., Dominik, C., Encrenaz, P., Fich, M., Fuente, A., Giannini, T., Goicoechea, J., de Graauw, T., Helmich, F., Herczeg, G., Jørgensen, J., Kristensen, L., Larsson, B., Lis, D., McCoey, C., Neufeld, D., Nisini, B., Olberg, M., Parise, B., Pearson, J., Plume, R., Risacher, C., Santiago, J., Saraceno, P., Tafalla, M., van Kempen, T., Visser, R., Wampfler, S., Yıldız, U., Ravera, L., Roelfsema, P., Siebertz, O., & Teyssier, D. 2010. Water abundance variations around high-mass protostars: HIFI observations of the DR21 region. *AaP*, **518**(July), L107.

van Dishoeck, E. F., Kristensen, L. E., Benz, A. O., Bergin, E. A., Caselli, P., Cernicharo, J., Herpin, F., Hogerheijde, M. R., Johnstone, D., Liseau, R.,

Nisini, B., Shipman, R., Tafalla, M., van der Tak, F., Wyrowski, F., Aikawa, Y., Bachiller, R., Baudry, A., Benedettini, M., Bjerkeli, P., Blake, G. A., Bontemps, S., Braine, J., Brinch, C., Bruderer, S., Chavarría, L., Codella, C., Daniel, F., de Graauw, T., Deul, E., di Giorgio, A. M., Dominik, C., Doty, S. D., Dubernet, M. L., Encrenaz, P., Feuchtgruber, H., Fich, M., Frieswijk, W., Fuente, A., Giannini, T., Goicoechea, J. R., Helmich, F. P., Herczeg, G. J., Jacq, T., Jørgensen, J. K., Karska, A., Kaufman, M. J., Keto, E., Larsson, B., Lefloch, B., Lis, D., Marseille, M., McCoey, C., Melnick, G., Neufeld, D., Olberg, M., Pagani, L., Panić, O., Parise, B., Pearson, J. C., Plume, R., Risacher, C., Salter, D., Santiago-García, J., Saraceno, P., Stäuber, P., van Kempen, T. A., Visser, R., Viti, S., Walmsley, M., Wampfler, S. F., & Yıldız, U. A. 2011. Water in Star-forming Regions with the Herschel Space Observatory (WISH). I. Overview of Key Program and First Results. *PASP*, **123**(Feb.), 138–170.